nature neuroscience

Article

https://doi.org/10.1038/s41593-025-02132-9

BOLD signal changes can oppose oxygen metabolism across the human cortex

Received: 18 December 2023

Accepted: 17 October 2025

Published online: 16 December 2025

Check for updates

Samira M. Epp[1,2,3], Gabriel Castrillón[1,2,4], Beijia Yuan[5], Jessica Andrews-Hanna[6,7], Christine Preibisch[2,8] & Valentin Riedl[1,2]

Functional magnetic resonance imaging measures brain activity indirectly by monitoring changes in blood oxygenation levels, known as the blood-oxygenation-level-dependent (BOLD) signal, rather than directly measuring neuronal activity. This approach crucially relies on neurovascular coupling, the mechanism that links neuronal activity to changes in cerebral blood flow. However, it remains unclear whether this relationship is consistent for both positive and negative BOLD responses across the human cortex. Here we found that about 40% of voxels with significant BOLD signal changes during various tasks showed reversed oxygen metabolism, particularly in the default mode network. These 'discordant' voxels differed in baseline oxygen extraction fraction and regulated oxygen demand via oxygen extraction fraction changes, whereas 'concordant' voxels depended mainly on cerebral blood flow changes. Our findings challenge the canonical interpretation of the BOLD signal, indicating that quantitative functional magnetic resonance imaging provides a more reliable assessment of both absolute and relative changes in neuronal activity.

Neuronal activity is the primary energy consumer in the brain, driven by oxygen metabolism and quantified as the cerebral metabolic rate of oxygen ($CMRO_2$)[1]. Functional magnetic resonance imaging (fMRI) maps this activity indirectly by detecting regional changes in blood oxygenation[2]. The resulting blood-oxygenation-level-dependent (BOLD) signal originates from fluctuations in deoxygenated hemoglobin, rather than from neuronal activity itself.

Interpreting BOLD signal changes (ΔBOLD) as changes in neuronal activity depends on neurovascular coupling, the process that links neuronal activity to local changes in cerebral blood flow (CBF)[3–7]. Classical work in human sensory cortices using positron emission tomography (PET) showed that sensory stimulation evokes modest increases in $CMRO_2$ but a disproportionately larger increase in CBF, resulting in a positive coupling ratio of $\Delta CBF/\Delta CMRO_2$ (n-ratio ~2–4)[8]. This surplus in CBF forms the basis of the canonical hemodynamic response (n-ratio > 1), which generally allows the interpretation of a positive BOLD response as increased neuronal activity and vice versa[9,10]. Mesoscopic studies have supported this principle by linking heightened neural or synaptic activity to increased CBF and positive BOLD responses[11–13]. Likewise, others have shown that inhibitory processes and decreased activity are linked to negative BOLD changes[14–18]. However, it remains unclear whether the canonical hemodynamic response applies uniformly beyond sensory cortices, particularly throughout the entire human cortex.

Several studies have shown that ΔBOLD does not always accurately reflect neuronal activity. Animal studies identified task-induced changes in CBF and metabolic activity, accompanied by minimal or opposite BOLD signal responses[19,20], indicating conditions where hemodynamics and neuronal activity are decoupled[4,21]. Reports of unchanged or even increased metabolism despite significant negative

[1]Institute of Neuroradiology, Uniklinikum Erlangen, Friedrich-Alexander-Universitat Erlangen-Nurnberg, Erlangen, Germany. [2]Institute of Neuroradiology, School of Medicine and Health, Technical University of Munich, Munich, Germany. [3]Graduate School of Systemic Neurosciences, Ludwig-Maximilians-Universität München, Munich, Germany. [4]Research Group in Medical Imaging, SURA Ayudas Diagnósticas, Medellin, Colombia. [5]Department of Physics, University of California, San Diego, CA, USA. [6]Department of Psychology, University of Arizona, Tucson, AZ, USA. [7]Cognitive Science, University of Arizona, Tucson, AZ, USA. [8]Clinic for Neurology, School of Medicine and Health, Technical University of Munich, Munich, Germany. e-mail: valentin.riedl@tum.de

https://doi.org/10.1038/s41593-025-02132-9

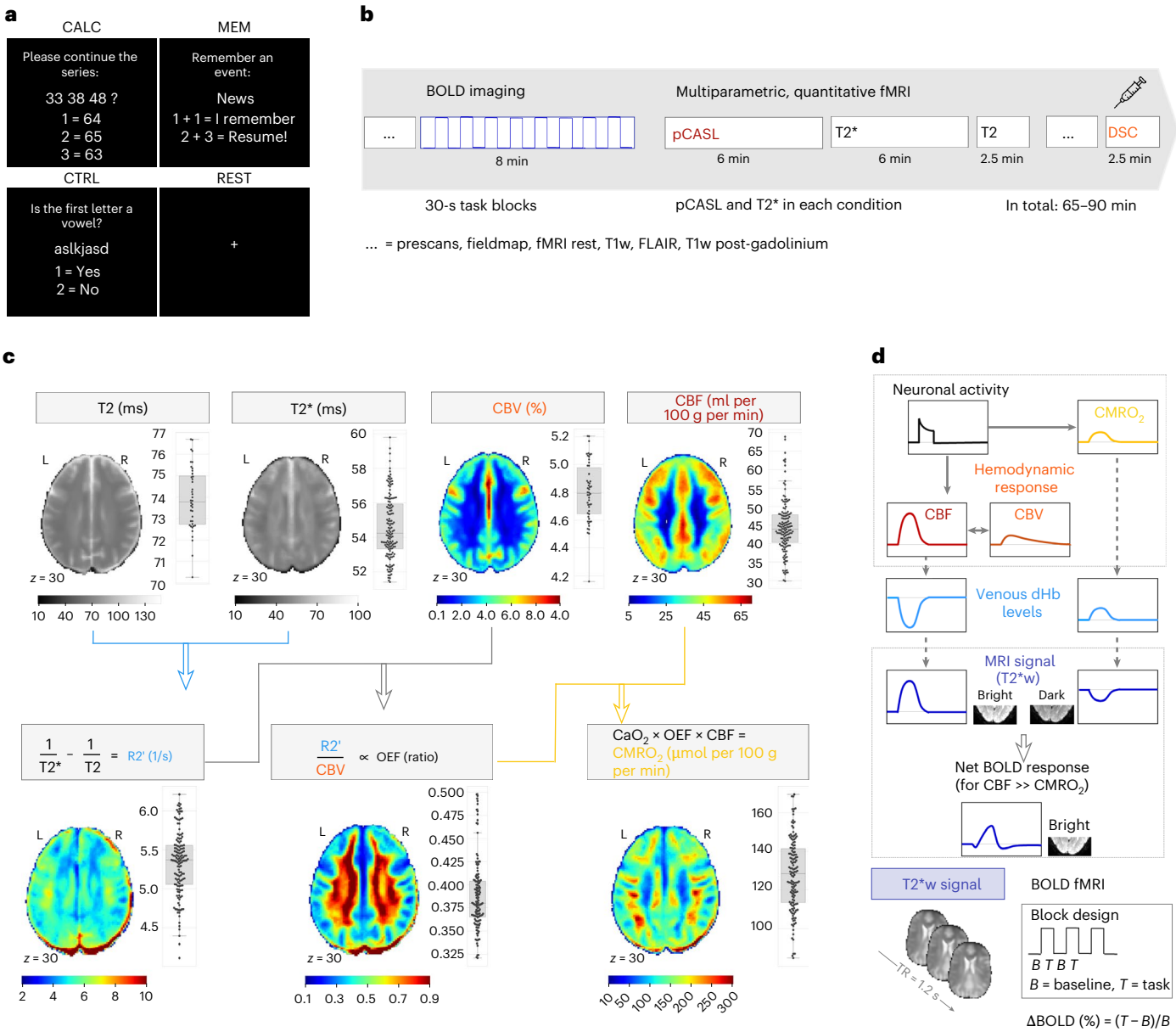


Fig. 1 | Study design, quantitative fMRI and the hemodynamic response model of BOLD fMRI. a, We performed BOLD and quantitative fMRI on healthy subjects performing four different conditions within the same imaging session: CALC, MEM, CTRL and REST. **b**, During each imaging session, we acquired BOLD fMRI data with a 30-s block design, together with multiparametric, quantitative fMRI data. Conditions were presented in pseudorandomized order: T2* mapping to measure both reversible and irreversible dephasing; pCASL to measure CBF during each condition; T2 mapping to measure irreversible dephasing due to tissue properties; and DSC MRI using a contrast agent to measure CBV during CTRL, at the end of the session. **c**, Quantitative fMRI delivers voxelwise $CMRO_2$ by integrating T2, T2*, CBV and CBF parameters via Fick's principle (see Methods section for detailed equations). Brain slices of subject-average parameter maps and boxplots illustrating average GM values across all 40 subjects and all conditions of the main study (line, median; box limits, upper and lower quartiles; whiskers, minimum and maximum data points except for outliers: values outside of 1.5 × interquartile range (IQR); individual dots, subject average per condition). R2′ reflects a voxel's overall dHb content. The OEF is proportional to R2′/CBV. Voxel-wise $CMRO_2$ is then calculated as the product of OEF, CBF and the arterial oxygen content of the blood (C_aO_2) as derived from individual measures of oxygen saturation and hematocrit. **d**, The canonical hemodynamic response model of the BOLD signal: increased neuronal activity leads to higher $CMRO_2$, which results in decreased oxygenation levels and an increased concentration of dHb in venous blood. Neurovascular coupling mechanisms initiate an increase in CBV and CBF. This hemodynamic response counteracts the effects of oxygen metabolism, ultimately leading to a decrease in dHb content. In BOLD fMRI, the net fluctuation of dHb levels is dynamically measured with T2*-weighted (T2*w) EPI. ΔBOLD during any task condition is calculated by subtracting task (*T*) from baseline (*B*) T2*w data. Based on the canonical hemodynamic response function, positive ΔBOLD are commonly interpreted as increased neuronal activity.

ΔBOLD or ΔCBF further challenge the assumption of uniform neurovascular coupling[22–25]. The BOLD signal itself reflects a complex interplay among changes in CBF, cerebral blood volume (CBV) and the oxygen extraction fraction (OEF) during capillary passage, making its interpretation region-dependent[10,26]. Consequently, various studies have reported inconsistencies between BOLD signal responses and cognitive or neuronal activity in humans[25,27–30]. Moreover, variations in vasculature[31] and hemodynamic responsiveness[9,31–34] can produce similar macroscopic BOLD patterns through distinct underlying mechanisms. These differences particularly affect the interpretation of BOLD signal patterns in patients with altered hemodynamics[10,30]. Together, these studies challenge the reliability of the BOLD signal response as

Table 1 | Whole-brain (gray matter) parameter values, mean±s.d. across 40 subjects and all conditions per subject

R2′ (1/s)	CBV (%vol)	OEF (ratio)	CBF (ml per 100 g per min)	$CMRO_2$ (μmol per 100 g per min)
5.3±0.4	4.8±0.2	0.39±0.04	44.5±7.2	127.8±18.4

an indicator of neuronal activity across the cortex, motivating a more quantitative examination of neurovascular coupling.

We addressed this question by measuring absolute oxygen metabolism and individual vascular components underlying positive and negative ΔBOLD. The gold standard for CBF and $CMRO_2$ measurements is ^{15}O PET; but this technique requires an on-site cyclotron, a sophisticated imaging setup and substantial experience in handling three different radiotracers (CBF, ^{15}O-water; CBV, ^{15}O-CO; OEF, ^{15}O-gas) of short half-lives[8,35]. Furthermore, this invasive method poses certain risks to participants owing to the exposure to radioactivity and arterial sampling. As an alternative, various MRI approaches have been developed over the past three decades to quantify voxel-wise oxygen extraction and metabolism in the human cortex[36–38]. The quantitative BOLD (qBOLD) approach is based on an analytical model[39] that relates R2′ to OEF[40–42]. A multiparametric variant of the qBOLD technique (mqBOLD) combines separate measurements of the intrinsic and effective relaxation times, T2 and T2* for reversible transverse relaxation rate (R2′), with an independent quantification of CBV for OEF measurement. mqBOLD imaging has been widely applied to study patient groups with vascular pathologies and brain tumors[42–47], summarized recently by ref. 36.

In this study, we used both quantitative and conventional BOLD imaging to test the hypothesis that ΔBOLD would not reliably reflect changes in oxygen metabolism throughout the entire cortex. We found that in a substantial fraction of voxels with significant BOLD responses, oxygen metabolism changes in the opposite direction to both positive and negative BOLD signals. Notably, these discordant voxels regulated oxygen demand primarily via changes in OEF, rather than CBF. These findings challenge the canonical hemodynamic response model, demonstrating that ΔBOLD alone can lead to misleading interpretations of underlying neuronal activity.

Results

Brain imaging data were collected using BOLD and quantitative fMRI while participants completed four experimental conditions within a single session (Fig. 1a,b). These conditions allowed identification of (1) 'task-positive' regions with increased BOLD signal and (2) 'task-negative' regions with negative BOLD response during calculation (CALC). We also examined (3) positive BOLD responses in the 'task-negative' regions during an autobiographical memory task (MEM). BOLD-contrast images for CALC and MEM were calculated relative to a controlled baseline task (CTRL) or an uncontrolled resting state (REST).

Quantitative fMRI, combining mqBOLD and pseudocontinuous arterial spin labeling (pCASL) MRI, estimates $CMRO_2$ as a metabolic marker of neuronal activity. $CMRO_2$ was calculated using Fick's principle, integrating parameter maps of several aspects of the hemodynamic response into a measure of oxygen metabolism (Fig. 1c and Methods). Table 1 lists parameter and $CMRO_2$ values averaged across all subjects and conditions.

The canonical hemodynamic response model (Fig. 1d) assumes an identical hemodynamic response across voxels, with ΔCBF exceeding $\Delta CMRO_2$ (n-ratio > 1). In this study, we used quantitative fMRI to measure hemodynamic parameters per condition and compared them to task-induced BOLD changes relative to an experimental baseline (ΔBOLD (%)).

Negative BOLD signal response does not indicate reduced oxygen metabolism

We performed separate partial least squares (PLS) analyses on BOLD and mqBOLD parameter maps to compare BOLD and quantitative fMRI results. Bootstrap ratios were used for statistical mapping (Fig. 2a shows CALC versus CTRL; additional contrasts in Supplementary Fig. 2). We found widespread significant positive and negative ΔBOLD for CALC versus CTRL. Group histograms (Fig. 2b) show task-related changes for each parameter within significant ΔBOLD regions (CALC-positive, CALC-negative). In CALC-positive masks, ΔCBF and $\Delta CMRO_2$ showed canonical amplitudes: ΔBOLD = 0.37%, ΔCBF = 6.5%, $\Delta CMRO_2$ = 3.1%, n-ratio ($\Delta CBF(\%)/\Delta CMRO_2(\%)$) = 2.1 (Fig. 2b). CALC-negative masks showed near-zero ΔCBF and $\Delta CMRO_2$, despite negative ΔBOLD reaching 70% of the positive amplitude (−0.26%). To address potential normalization distortions, we also analyzed native-space data using individual BOLD masks, confirming robust positive ΔCBF and $\Delta CMRO_2$ in CALC-positive masks, with no significant response in CALC-negative masks across subjects (Fig. 2c). A second-level GLM model (Supplementary Fig. 1a,b), instead of the PLS approach, confirmed near-zero changes of median ΔCBF and $\Delta CMRO_2$ in CALC-negative masks. Overall, positive ΔBOLD values matched the canonical hemodynamic response, with ΔCBF (in %) being at least ten times higher than ΔBOLD and twice the amplitude of $\Delta CMRO_2$ (n-ratio > 2). However, no significant negative ΔCBF, ΔCBV, ΔT2* or $\Delta CMRO_2$ were found in negative ΔBOLD masks across subjects.

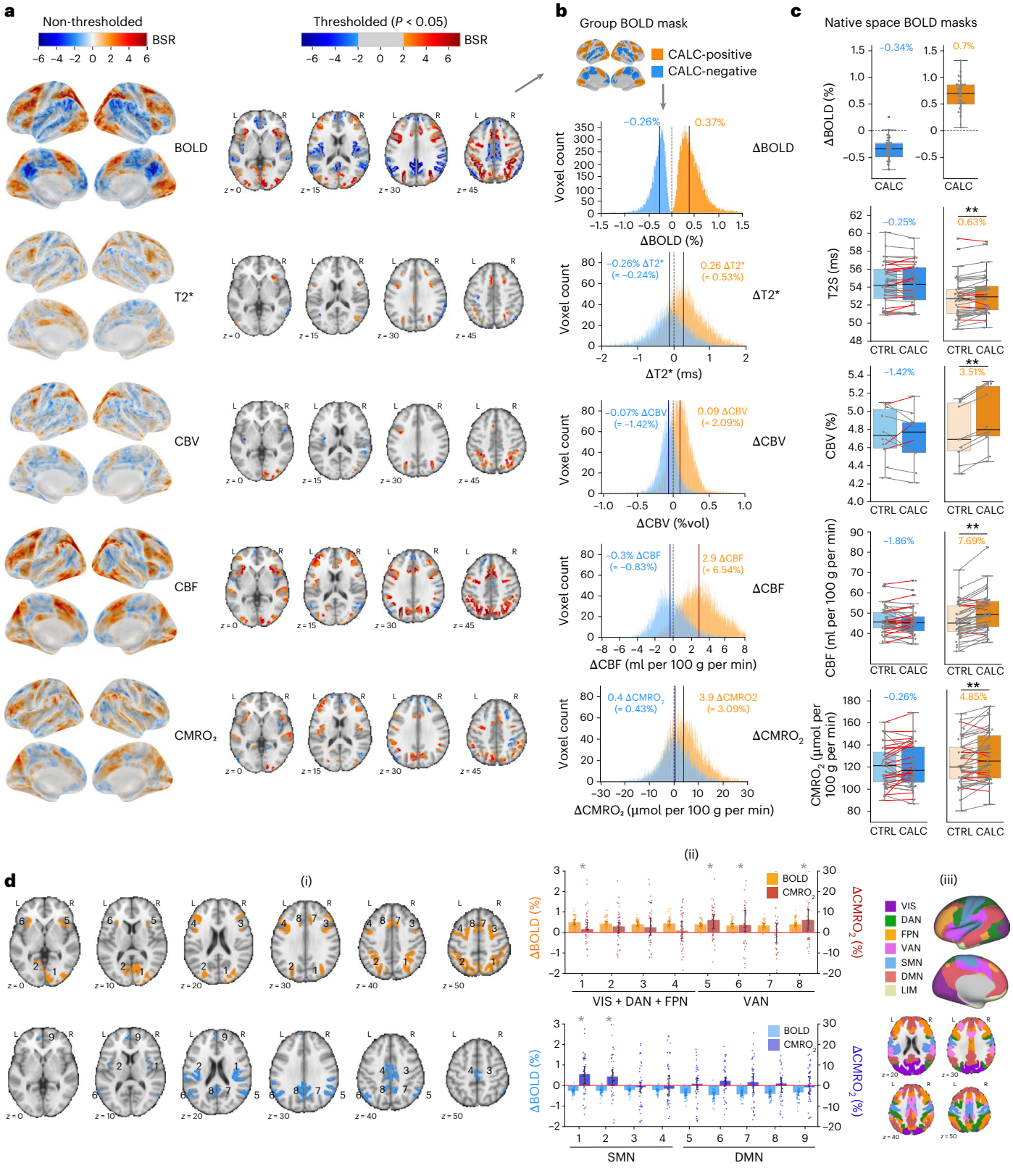
We then analyzed metabolic parameters regionally, avoiding brain-wide averaging effects. Eight clusters showed positive ΔBOLD, and nine clusters showed negative ΔBOLD (Fig. 2d(i)). Median $\Delta CMRO_2$ was significantly positive in half of the positive ΔBOLD clusters but negative in none of the negative clusters (Fig. 2d(ii)). Notably, two auditory network clusters (SMN 1, SMN 2) with negative ΔBOLD had significant positive $\Delta CMRO_2$.

Fig. 2 | Negative ΔBOLD does not indicate reduced oxygen metabolism. All analyses across N = 40 subjects of the main study, CBV results across N = 10. **a**, Statistical results of the PLS group analysis in standard MNI space, comparing CALC and CTRL, for both BOLD and quantitative fMRI parameter maps. Maps projected on the brain surface show non-thresholded bootstrap ratios (BSRs) (akin to z values) of the first latent variable, which was significant in each analysis: that is, for BOLD, CBF, CBV (N = 10), T2* and $CMRO_2$, respectively (permutation tests, P < 0.001). Red voxels indicate higher values during CALC compared to CTRL, and blue voxels represent the opposite contrast. Axial slices display significant brain clusters, thresholded at BSR ± 2 (akin to P < 0.05, cluster size > 30 voxels) for each parameter. **b**, Histograms depict group-average median voxel distributions of all parameters (CALC minus CTRL) within the binarized CALC-positive and CALC-negative group masks (shown as surface plot). **c**, Subject distribution of all parameters in native space. Dots represent individual subject values, calculated as the median across voxels within individual BOLD masks of significant positive (orange) and negative (blue) ΔBOLD. Boxplots: line, median; box limits, upper and lower quartiles; whiskers, minimum and maximum data points except for outliers: values outside of 1.5 × IQR; individual dots, one dot per subject, median voxel values. Paired samples, two-sided t-tests, $^{**}P$ < 0.001. Gray lines connect values obtained from individual subjects, and red lines indicate subjects where the direction of ΔCBF or $\Delta CMRO_2$ deviates from what the BOLD signal suggests. **d**, Regional clusters (i; designated by numbers) of positive (top) and negative (bottom) ΔBOLD (PLS group results, thresholded at BSR > ±3). (ii), associated bar plots showing ΔBOLD and $\Delta CMRO_2$. Please note the different axes for ΔBOLD and $\Delta CMRO_2$. Bars indicate ΔBOLD (%) and $\Delta CMRO_2$ (%) median across voxels, error bars 95% CI, 2,000 bootstraps; and dots represent subject values. Any signal increase or decrease for which error bars cross the zero line is considered nonsignificant; an asterisk denotes P < 0.05, not corrected for multiple comparisons. (iii), Clusters are located in different functional networks, as depicted on the brain surface and in axial slices[79]. Yeo networks: DAN, dorsal attention; FPN, frontoparietal; L, left; R, right; SMN, somatomotor; VAN, ventral attention; VIS, visual; LIM, limbic network.

https://doi.org/10.1038/s41593-025-02132-9

Control analyses

We also examined ΔBOLD and $\Delta CMRO_2$ for the other contrasts, CALC versus REST (Supplementary Fig. 2a–c) and MEM versus CTRL (Supplementary Fig. 2d–g). CALC-positive and CALC-negative masks showed higher overall ΔBOLD, ΔT2*, ΔCBF and $\Delta CMRO_2$ compared to CTRL, but changes within CALC-negative masks remained nonsignificant (Supplementary Fig. 2c). For the MEM task, results mirrored the CALC patterns, with similar BOLD signal amplitudes and stronger positive than negative ΔBOLD. However, ΔCBF and $\Delta CMRO_2$ were significant only in the MEM-positive mask. Thus, positive ΔBOLD reliably indicated significant positive $\Delta CMRO_2$ across conditions, but the metabolic interpretation of negative ΔBOLD remained unclear. Supplementary Table 1 summarizes average parameter changes for all conditions.



Several factors could explain the absence of hemodynamic and metabolic changes, especially related to negative ΔBOLD: (1) voxel-specific signal confounds, (2) limited sensitivity for detecting negative ΔCBF or $\Delta CMRO_2$ or (3) distinct hemodynamic mechanisms in certain regions. We address each explanation below.

Most MEM-positive voxels overlapped with the default mode network (DMN), which showed negative ΔBOLD during CALC (Supplementary Fig. 2f). To test for voxel-specific confounds, we analyzed CBF and $CMRO_2$ in voxels occurring in both MEM-positive and CALC-negative masks. Supplementary Fig. 2h shows the histograms of ΔBOLD, ΔCBF and $\Delta CMRO_2$ for all voxels of a conjunction mask (MEM-positive ∧ CALC-negative). For positive ΔBOLD (0.32%), we observed a canonical increase in ΔCBF (5.94%) and $\Delta CMRO_2$ (3.54%). However, in the same voxels, a negative ΔBOLD (−0.29%) was associated with a much weaker ΔCBF (−0.47%), resulting in a positive $\Delta CMRO_2$ (1.68%). Thus, a lower ΔCBF than expected from the canonical framework results in negative ΔBOLD for elevated $\Delta CMRO_2$. Crucially, the absence of canonical negative BOLD responses in 'conjunction voxels' cannot be explained by voxel-specific confounds, as those same voxels do display a canonical response for positive ΔBOLD.

According to the hemodynamic response model (Fig. 1d), neurovascular coupling is primarily driven by changes in CBF. To validate the sensitivity of pCASL imaging for detecting ΔCBF, we performed several control analyses (Supplementary Fig. 3). We found ΔCBF magnitudes ranging from −9% to +27%, with regions of positive ΔCBF showing higher *n*-ratios than those with negative ΔCBF (Supplementary Fig. 3a). Moreover, the spatial pattern of negative ΔCBF during CALC matched that observed with PET from a different study (Supplementary Fig. 3b). Notably, CBF decreases identified by PET and MRI were more localized than BOLD decreases and centered on peak regions. Additionally, we also validated the homogeneity of our MRI-derived OEF with independent PET data (Supplementary Fig. 3c).

We also assessed signal stability of BOLD and CBF measurements during continuous task performance. In the main study (Fig. 1), block durations vary for BOLD (30 s) and quantitative (~6 min) fMRI to achieve the best signal-to-noise ratio (SNR) for each modality. In a control study ($N = 18$), participants performed 3-min CALC and MEM blocks while BOLD data were collected. BOLD signals remained stable without habituation or drift (Supplementary Fig. 3d), with amplitude changes comparable to the main study (CALC-positive/negative/MEM-positive: 0.6%/−0.46%/0.34% versus 0.70%/−0.34%/0.51%). Time-resolved pCASL analysis from the main study also showed constant CBF data throughout measurement blocks (Supplementary Fig. 3e).

High prevalence of discordant voxels among positive and negative BOLD responses

We next assessed the ΔBOLD–$\Delta CMRO_2$ relationships on the voxel level and compared our data to an established model of hemodynamic responses. The Davis model predicts ΔBOLD responses based on realistic cortical ranges for $\Delta CMRO_2$(%) and ΔCBF(%)[48]. Figure 3a displays the model's prediction of ΔBOLD (contours, −3% to +3%) for a set of typical hemodynamic response parameters. A canonical BOLD response occurs when ΔCBF exceeds $\Delta CMRO_2$ (*n*-ratio > 1). However, the model also predicts discordant responses—where ΔBOLD disagrees with metabolic change—when ΔCBF is lower than $\Delta CMRO_2$ (*n*-ratio < 1) or their signs differ (Fig. 3a, violet shading). For example, a negative ΔBOLD of −1.3% would arise if CBF increased by only about 5% during a $\Delta CMRO_2$ of +23%. In other words, the same metabolic change can result in opposite signs of the BOLD signal, depending on the magnitude of related ΔCBF. Because we measured all relevant parameters and calculated $\Delta CMRO_2$ using Fick's principle, we next compared our empirical data to the model predictions.

Figure 3b presents subject-averaged voxel data for CALC versus CTRL, colored by positive/negative ΔBOLD (Supplementary Fig. 4a for CALC versus REST and Supplementary Fig. 4b for MEM versus CTRL). To mitigate low SNR at the voxel level, $\Delta CMRO_2$ was calculated using more stable ΔR2′ data from BOLD fMRI (see Methods and Supplementary Fig. 5 for sensitivity analysis). Our empirical data support several predictions of the Davis model: positive ΔBOLD voxels cluster above the line with a slope of 1, indicating an *n*-ratio > 1. We also identify a substantial number of discordant voxels: those with opposite ΔBOLD and $\Delta CMRO_2$. Those can be summarized as red voxels on the left and blue voxels on the right side of zero $\Delta CMRO_2$ (Fig. 3b, red dashed line). Interpreting the activity in discordant voxels using only BOLD data and assuming a uniform canonical response would lead to substantial misinterpretation.

To highlight the number of discordant responses, we plotted CALC-positive (Fig. 3c, top) and CALC-negative (Fig. 3c, bottom) voxels separately, highlighting discordant voxels (violet shading). Discordant voxels account for 31% and 66% of positive and negative ΔBOLD, respectively (Fig. 3c, pie charts); with a similar ratio of discordant negative ΔBOLD within the DMN (pie chart 'DMN only'), the network with the most consistently reported negative BOLD signal responses. Moreover, discordant voxels are spatially distributed across the cortex (Fig. 3c, brain slices) and occur equally among voxels from the lowest to highest quartile of BOLD signal amplitudes (Fig. 3c, bar plots). We repeated these analyses for CALC versus REST (Supplementary Fig. 4a) and MEM versus CTRL (Supplementary Fig. 4b). Again, discordant voxels appeared with a uniform cortical distribution and across the full range of ΔBOLD, amounting to 36%/52% of significant positive/negative ΔBOLD voxels in CALC versus REST and 12%/54% in MEM versus CTRL.

Figure 3d summarizes voxel median parameter values separately for concordant and discordant voxels. Concordant voxels with either positive or negative ΔBOLD demonstrate a canonical hemodynamic response (*n*-ratio 2.0 for positive, 1.6 for negative ΔBOLD; Fig. 3d, yellow and turquoise bars). Discordant voxels, however, show ΔBOLD opposite to their metabolic response and lower than expected ΔCBF (Fig. 3d, violet bars). Notably, discordant ΔBOLD occurred in about one-third of positive and two-thirds of negative ΔBOLD voxels across different tasks and all magnitude ranges, distributed evenly throughout the cortex.

Potentially, discordance between ΔBOLD and $\Delta CMRO_2$ could result from partial volume effects when integrating voxel data from imaging sequences with heterogeneous voxel sizes, as occurred in our main study. To address this, we conducted a replication study ($N = 10$) using harmonized acquisition matrices for BOLD and mqBOLD data. Results mirrored the main study (Supplementary Fig. 6): 40% of all voxels with either significant positive or negative ΔBOLD were classified as discordant, and discordant voxels again showed smaller CBF responses than expected from canonical neurovascular coupling.

Finally, we directly estimated the parameters of the Davis model using our own data. With measurements of ΔBOLD, CBV, OEF and CBF, we calculated α and each subject's calibration factor M empirically. The average values were $\alpha = 0.38$ and $M = 11.2 \pm 1\%$ ($N = 40$). Supplementary Fig. 7 replicates Fig. 3 using the Davis model parameters instead of Fick's formula to quantify $CMRO_2$.

'Mixed' voxels switch between concordant and discordant BOLD responses across tasks

Next, we examined whether voxels with both positive and negative BOLD responses during CALC or MEM (using the conjunction mask of the control analysis in Supplementary Fig. 2h) exhibit consistent hemodynamic response patterns for both signs of ΔBOLD. Voxels were classified as 'concordant only', 'discordant only' or 'mixed' based on whether BOLD and metabolic responses matched in both tasks, differed in both tasks or showed a mixed pattern (Fig. 4a). The pie chart illustrates that most voxels (48%) were 'mixed', and 35% and 18% were consistently concordant or discordant, respectively. Figure 4b displays the spatial and amplitude distributions for ΔCBF and $\Delta CMRO_2$ across the three categories. 'Concordant only' voxels showed canonical

https://doi.org/10.1038/s41593-025-02132-9

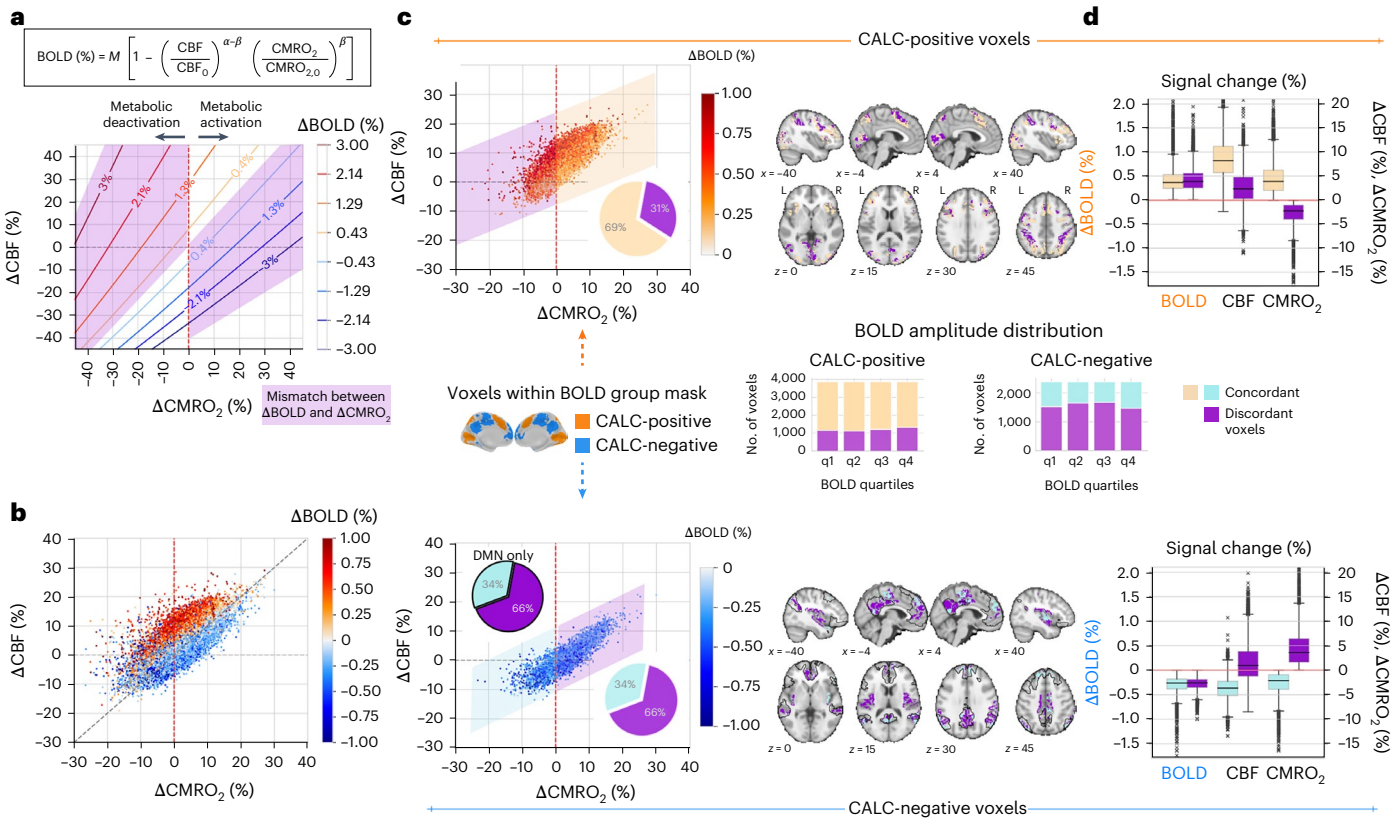


Fig. 3 | Dependence of BOLD signal responses on changes in CBF and $CMRO_2$. **a**, Visualization of the Davis model. Predicted BOLD responses (ΔBOLD (%)) are depicted as colored contour lines across ΔCBF (%) and $\Delta CMRO_2$ (%). The model illustrates that for a given $\Delta CMRO_2$(%), the direction and magnitude of the BOLD response depend on the amplitudes of ΔCBF(%). The canonical hemodynamic response assumes that an increase in ΔCBF will exceed the increase in $\Delta CMRO_2$, resulting in a positive ΔBOLD and vice versa for negative ΔBOLD. However, the Davis model also predicts a range of BOLD responses with discordant signs compared to the changes in underlying metabolic activity (violet shading). **b**, Empirical data from BOLD and quantitative fMRI for all cortical voxels, median across $N = 40$ subjects of the main study. $\Delta CMRO_2$ was calculated from BOLD-derived ΔR2′ (Methods), median across all subjects per voxel, with colors indicating ΔBOLD (%). Our experimental data replicate the slope and range of values predicted by the Davis model, particularly demonstrating a substantial number of voxels with ΔBOLD opposing $\Delta CMRO_2$. **c**, Voxels representing the median across $N = 40$ subjects from the main study display significantly positive (top) and negative (bottom) BOLD responses from **b**. Voxels with ΔBOLD concordant to $\Delta CMRO_2$ are highlighted on a light yellow/turquoise background, and voxels with discordant ΔBOLD values are shown on a violet background. The pie charts illustrate the ratio of discordant to concordant voxels. Bottom, the pie chart with black contours specifically summarizes the ratio of discordant voxels within the DMN. Axial slices illustrate the spatial distribution of significantly concordant and discordant BOLD voxels, with black contours indicating the DMN. Right, center, stacked bars illustrate the amplitude distribution of discordant and concordant voxels across BOLD amplitude quartiles. It is noteworthy that discordant voxels show neither spatial nor amplitude preference. **d**, The boxplots summarize $\Delta CMRO_2$ (%) and ΔCBF (%) across all voxels, median across $N = 40$ subjects of the main study, with either concordant or discordant ΔBOLD (%); (line, median; box limits, upper and lower quartiles; whiskers, minimum and maximum data points except for outliers: values outside of 1.5 × IQR; based on median voxel values across subjects). Please note that discordant and concordant voxels exhibit similar ΔBOLD amplitude distributions, even though they signal opposite metabolic responses.

hemodynamic responses (n-ratio ~2) regardless of BOLD sign or task (yellow/turquoise bars), and 'discordant only' voxels lacked canonical responses for either direction (violet/lilac bars). 'Mixed' voxels exhibited canonical coupling for positive BOLD, but not for negative BOLD (red/orange bars). Because changes in $CMRO_2$, which are not modulated by CBF, must be matched by OEF changes, we tested whether baseline OEF varies by voxel type. We hypothesized that 'discordant only' voxels, with the lowest ΔCBF during a task, would have the lowest baseline OEF (indicating the highest oxygen buffer). In line with this hypothesis, baseline OEF was lowest in 'discordant only' voxels, intermediate in 'mixed' and highest in 'concordant only' voxels (Fig. 4c), suggesting that discordant voxels compensate for higher oxygen demand mainly via OEF changes. Importantly, OEF data were independently acquired from CBF data.

Baseline OEF predicts different hemodynamic response types

We next examined baseline hemodynamics across the cortex by pooling all voxels with significant ΔBOLD during either task (CALC, MEM)—comprising 53% of all gray matter (GM) voxels—and categorizing them as concordant, discordant or not task-involved (Fig. 5a(i)). Regression plots show that baseline $CMRO_2$ correlates linearly with CBF, OEF and CBV across all voxel groups, consistent with Fick's principle. Multiple linear regression analyses using all three parameters showed that baseline OEF accounted for >68% of $CMRO_2$ variance, followed by CBF (>28%) and CBV (>1%), with similar model parameters for concordant and discordant voxels (concordant model: $F(3,21{,}809) = 72{,}070$, $P < 0.001$, $CMRO_2 = 139.9 + 321.1 \times OEF + 3.3 \times CBF + 0.4 \times CBV + e$, $R^2 = 0.91$; discordant model: $F(3,14{,}544) = 48{,}390$, $P < 0.001$, $CMRO_2 = 128.1 + 309.2 \times OEF + 3.2 \times CBF + 1.3 \times CBV + e$; $R^2 = 0.91$; all predictors mean-centered, $P < 0.001$ for all beta values). According to the $CMRO_2$ model parameter, discordant voxels have a lower baseline metabolism, whereas concordant voxels have significantly higher baseline CBF and OEF but lower CBV (Fig. 5b).

To validate lower OEF and higher CBV in discordant voxels, we analyzed two external quantitative susceptibility mapping (QSM) datasets (Fig. 5c). Projecting our voxel masks onto these data, we observed that

https://doi.org/10.1038/s41593-025-02132-9

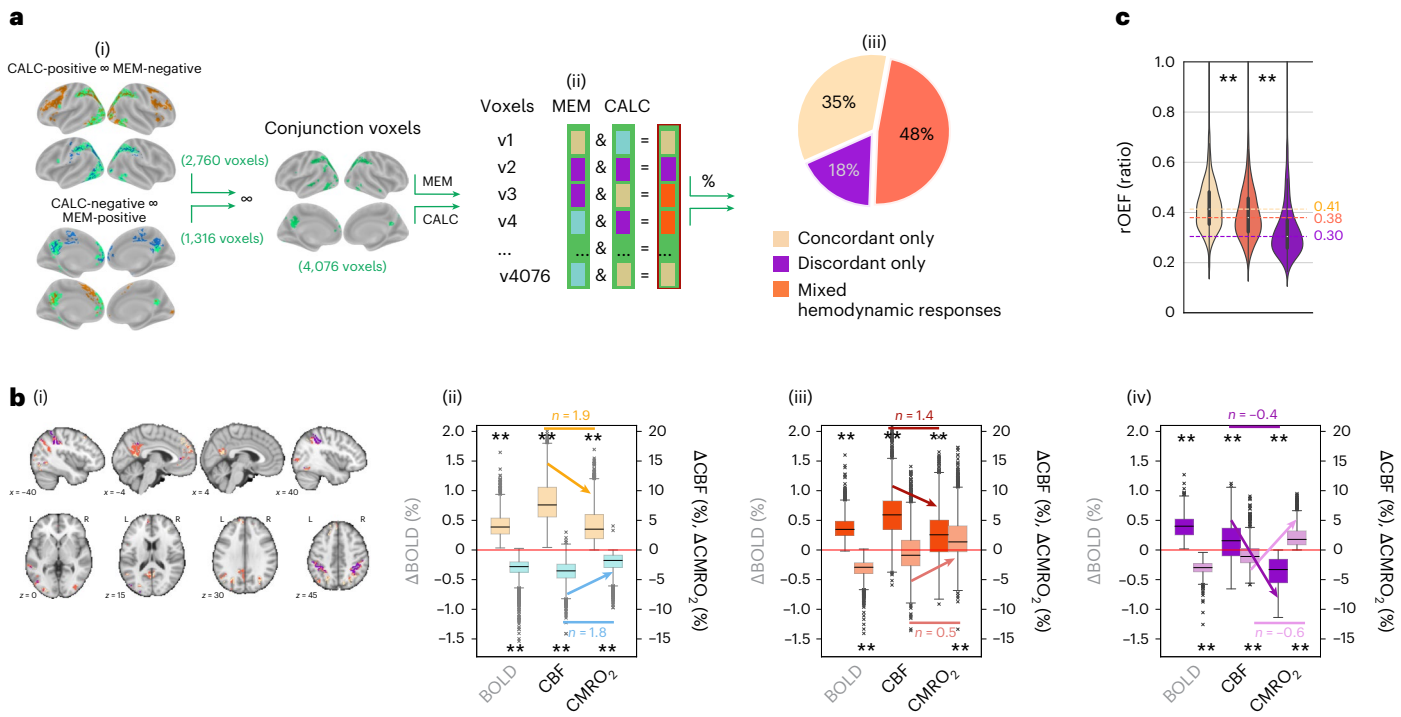


Fig. 4 | Concordant or discordant BOLD signal responses depend on baseline OEF. Median voxel values across $N = 30$ subjects of the main study. **a**, Conjunction voxels (i; green outlines) display both positive and negative changes in BOLD signal during the CALC and MEM conditions. (ii), these voxels were categorized based on their response types. (iii), the pie chart summarizes the consistency of these response types across voxels: 35% of all conjunction voxels showed concordant responses, meaning they had the same sign of ΔBOLD and $\Delta CMRO_2$ during both MEM and CALC conditions ('concordant only'); 18% of all conjunction voxels showed discordant responses in both conditions ('discordant only'); 48% of the conjunction voxels ('mixed' voxels) showed concordant responses in one condition and discordant responses in the other. **b**, The spatial distribution (i) of voxel categories is illustrated on brain slices with consistent color overlays: 'concordant only' and 'mixed' voxels primarily cluster in regions of the DMN, and 'discordant only' voxels occur in the medial part of the VAN. The boxplots display subject-median parameter values separately for 1,410 'concordant only' (ii), 1,943 'mixed' (iii) and 723 'discordant only' voxels (iv) (line, median; whiskers, minimum and maximum data points except for outliers: values outside of 1.5 × IQR; based on median voxel values across subjects). Although the range of ΔBOLD is similar across the three categories, ΔCBF and $\Delta CMRO_2$ vary strongly as expressed by their n-ratios. Asterisks indicate significant differences from zero, tested via independent t-tests, two-sided, corrected for multiple comparisons. **c**, The three voxel categories exhibit significantly different OEF during CTRL baseline, with 'concordant only' voxels having significantly higher OEF and 'discordant only' voxels having significantly lower OEF than 'mixed' voxels. $^{**}P < 0.001$, independent-sample permutation test on the median values, two-sided, conducted for 'mixed' versus the two other voxel types, 2,000 permutations. rOEF, relative OEF.

discordant voxels had slightly but significantly lower susceptibility (indicating lower deoxyhemoglobin (dHb)) and significantly higher venous density, supporting our findings.

Finally, we investigated whether ΔOEF might serve as an alternative mechanism to ΔCBF in accommodating oxygen demand during task processing. Regression plots show the linear correlation between $\Delta CMRO_2$ and ΔCBF, ΔOEF and ΔCBV, separately for concordant and discordant voxels, illustrating the significant contribution of each hemodynamic parameter to oxygen metabolism (Fig. 5d). However, we also identified two distinct patterns of hemodynamic responses. Multiple linear regression analyses revealed that in concordant voxels, $\Delta CMRO_2$ was mainly driven by ΔCBF (concordant model: $F(2,21,971) = 67,980$, $P < 0.001$, with ΔCBF explaining 87% and ΔOEF 16% of a total explained variance of $R^2 = 0.86$ of the model: $\Delta CMRO_2(\%) = 2.6 + 0.83 \times \Delta OEF(\%) + 0.86 \times \Delta CBF(\%) + e$; all predictors mean-centered, $P < 0.001$ for all beta values). In discordant voxels, ΔOEF was the primary regulator, with ΔCBF secondary (discordant model: $F(2,14,694) = 39,320$, $P < 0.001$, with ΔOEF explaining 58% and ΔCBF 42% of a total explained variance of $R^2 = 0.84$ of the model: $\Delta CMRO_2(\%) = 1.2 + 1.1 \times \Delta OEF(\%) + 0.88 \times \Delta CBF(\%) + e$; all predictors mean-centered, $P < 0.001$ for all beta values). The negative $\Delta CMRO_2$ – ΔOEF correlation for concordant voxels reflects compensatory oxygenation during ΔCBF surplus (Fig. 5d, center). CBV was not included in these regressions, as ΔCBV was only acquired for the CALC–CTRL contrast. In summary, concordant voxels regulate $CMRO_2$ mostly via ΔCBF (87%), whereas discordant voxels rely more on ΔOEF (58%) compared to ΔCBF (42%).

Discussion

In this study, we evaluated the consistency between changes in the BOLD signal and oxygen metabolism in GM voxels across the human cortex. This would support the common interpretation of positive and negative ΔBOLD as indicators of increased or decreased neuronal activity. Contrary to the canonical BOLD response model, we found that approximately 40% of brain voxels with significant ΔBOLD exhibited opposing changes in oxygen metabolism. Specifically, voxels with positive ΔBOLD showed decreased $\Delta CMRO_2$, whereas those with negative ΔBOLD exhibited increased $\Delta CMRO_2$. By measuring the BOLD signal, CBF, OEF and $CMRO_2$ in the same session, we uncovered distinct neurovascular mechanisms in regions with concordant versus discordant responses. Discordant voxels primarily regulate oxygen demand via ΔOEF, whereas concordant voxels display a larger increase in ΔCBF, aligning with canonical predictions. Moreover, discordant voxels demonstrated lower baseline $CMRO_2$ and OEF, indicating that their baseline oxygen supply is sufficient to meet higher metabolic demands. In conclusion, we identified two distinct hemodynamic responses to neuronal activity changes, influenced by baseline OEF and metabolism.

https://doi.org/10.1038/s41593-025-02132-9

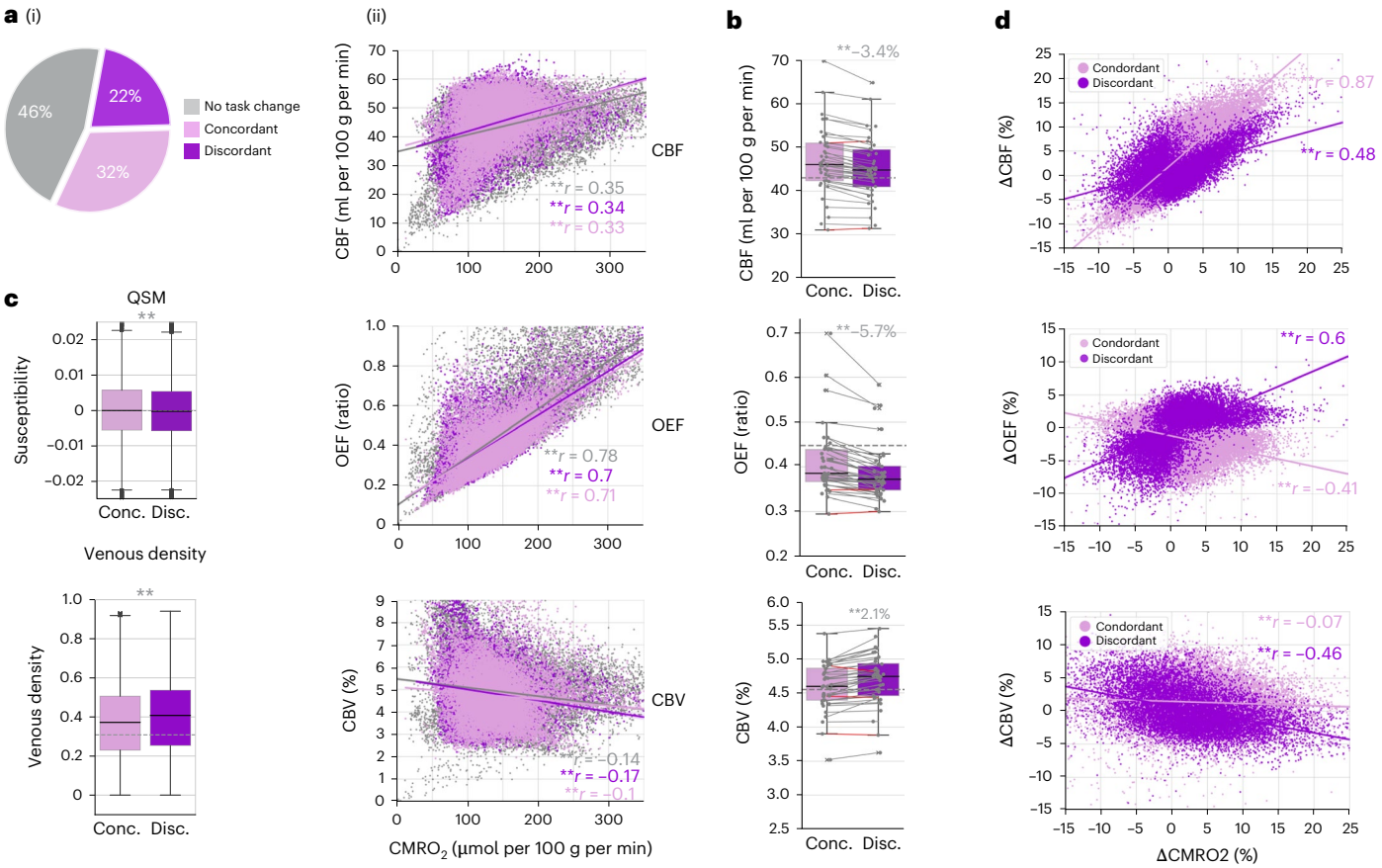


Fig. 5 | Two types of hemodynamic responses via changes in CBF or OEF. **a**, Across all task conditions, 22% of all GM voxels showed discordant and 32% showed concordant responses, and 46% were not significantly involved in any task (i). Regression plots (ii): during baseline, $CMRO_2$ and CBF show a moderate correlation (Pearson's $r > 0.32$, $P < 0.001$), $CMRO_2$ and OEF are highly correlated ($r > 0.7$, $P < 0.001$), and $CMRO_2$ and CBV show a weak negative correlation ($r < -0.1$, $P < 0.001$) across all groups of voxels; voxel medians across 40 subjects. **b**, In CTRL baseline, across all 40 subjects, discordant voxels, on average, show significantly lower CBF (−3.4%), lower OEF (−5.7%) and higher CBV (2.1%) than concordant voxels (paired samples, two-sided *t*-test, $P < 0.001$). Boxplots: line, median; box limits, upper and lower quartiles; whiskers, minimum and maximum data points except for outliers: values outside of 1.5 × IQR; individual dots, median subject values across voxels; gray line, median of remaining GM voxels. **c**, Marginally but significantly lower baseline susceptibility (QSM) and higher venous density in discordant versus concordant voxels, revealed by two external datasets[68,69]. Boxplots: line, median; box limits, upper and lower quartiles; whiskers, minimum and maximum data points except for outliers: values outside of 1.5 × IQR; based on voxel values; gray line, median of remaining GM voxels. $^{**}P < 0.001$, independent samples permutation test on the median values, two-sided, conducted for discordant versus concordant voxels, 2,000 permutations. **d**, Correlation of $\Delta CMRO_2$(%) with either ΔCBF(%), ΔOEF(%) or ΔCBV(%) across all task contrasts (CALC versus CTRL, voxel median across 40 subjects; MEM versus CTRL, voxel median across 30 subjects), separately for concordant (pale) and discordant (dark violet) voxels. $\Delta CMRO_2$ and ΔCBF showed a strong positive correlation across concordant voxels ($r = 0.87$, $P < 0.001$) and a moderate correlation across discordant voxels ($r = 0.48$, $P < 0.001$). In contrast, $\Delta CMRO_2$ and ΔOEF showed a moderate, positive correlation across discordant voxels ($r = 0.60$, $P < 0.001$) and a weak, negative correlation across concordant voxels ($r = -0.41$, $P < 0.001$). ΔCBV could only be evaluated for a subset of 10 subjects and only across the CALC versus CTRL contrast (Methods). $\Delta CMRO_2$ and ΔCBV showed a weak correlation around zero across concordant voxels ($r = -0.07$) and a moderate, negative correlation across discordant voxels ($r = -0.46$, $P < 0.001$). Conc., concordant; Disc., discordant.

Canonical hemodynamic response for average positive ΔBOLD

We combined BOLD with quantitative fMRI to investigate hemodynamic and metabolic changes in relation to ΔBOLD. Participants performed cognitive tasks eliciting both positive and negative BOLD signal responses across the cortex. Specifically, we aimed to elicit both response types in identical voxels, facilitating a direct comparison of their hemodynamic responses. We employed a cognitively demanding calculation task that induced positive ΔBOLD in various attention-related regions[49,50] while concurrently inducing negative ΔBOLD in DMN regions[50,51]. Additionally, participants undertook an autobiographical memory task known to induce positive ΔBOLD in DMN regions, partially overlapping with those of negative ΔBOLD during CALC[52,53]. This allowed us to examine opposing ΔBOLD within the same voxels.

Our study also addressed the implications of differing baseline states. Although BOLD signal responses to cognitive tasks are usually compared against low-level control tasks[53–55], negative ΔBOLD was often reported in comparison to an uncontrolled resting state[51,56]. Consequently, we included both baseline types into the study design, and all experimental conditions successfully elicited anticipated BOLD signal responses. On average, negative BOLD signal responses constituted approximately 50–70% of the amplitude of positive ΔBOLD (Fig. 2). Additionally, ΔBOLD was larger when compared to REST than to CTRL baseline (Supplementary Table 1 and Supplementary Fig. 2a–c).

Compared to BOLD fMRI, which requires subtraction analyses between conditions, the mqBOLD approach provides quantitative measures for each condition. During CTRL baseline, we observed average GM values of $CMRO_2$ and hemodynamic parameters (Table 1) consistent with existing literature on the healthy human brain[35,38,42,51,57–59]. Likewise, task-related changes (Supplementary Table 1) aligned with prior findings[58,60,61], where $\Delta CMRO_2$ and ΔCBF exceeded positive ΔBOLD by factors of 10–20, yielding an *n*-ratio of

approximately 2 (Fig. 2) and thereby conforming to the canonical hemodynamic response[10,62].

Discordant hemodynamics for negative ΔBOLD and in regions with positive ΔBOLD

Despite a canonical hemodynamic response for mean positive ΔBOLD, we did not find significant hemodynamic or metabolic changes for negative ΔBOLD (see CALC versus CTRL, Fig. 2c) for either task condition (see MEM versus CTRL, Supplementary Fig. 2g) or when comparing against REST baseline (Supplementary Fig. 2c). In a region-specific analysis, we also observed significant deviations from the canonical response in four out of eight clusters with positive ΔBOLD (Fig. 2d). One could argue that voxels with discordant ΔBOLD might suffer from voxel-specific artifacts such as partial volume effects or differences in vasculature, leading to insignificant ΔCBF. To address this issue, we designed our study to achieve significant ΔBOLD during both CALC and MEM tasks in identical voxels, facilitating within-voxel comparisons of ΔBOLD and quantitative measures. Among these voxels (Supplementary Fig. 2h, 'conjunction voxels'), we observed only weak ΔCBF (−0.5%) for negative ΔBOLD but strong positive ΔCBF (5.9%) for positive ΔBOLD, despite similar ΔBOLD amplitudes (−0.29% and 0.32%). For this voxel subset, discordant negative ΔBOLD is unlikely due to artifacts, as a canonical hemodynamic response was confirmed for positive ΔBOLD.

In summary, we identified a canonical hemodynamic response for mean positive ΔBOLD, but inconsistencies in certain regions. For negative ΔBOLD, we did not find significant negative ΔCBF or $\Delta CMRO_2$ across subjects. Our findings align with previous animal studies indicating inconsistent hemodynamic responses in cortical and subcortical regions[31,34,63].

Validation of discordant hemodynamics using the Davis model and replication data

On the voxel level, we evaluated our findings in comparison to a well-established model of cerebral hemodynamic responses (Fig. 3). The Davis model predicts BOLD signal amplitudes for realistic ranges of $\Delta CMRO_2$ and ΔCBF in the human brain[48]. Despite it being published more than 20 years ago, no study has examined the model's accuracy across the human cortex. Intriguingly, the Davis model predicts a range of discordant positive and negative ΔBOLD for biologically plausible ΔCBF in relation to $\Delta CMRO_2$ (Fig. 3, violet shading and voxels). Our empirical findings (Fig. 3b) align closely with these predictions using established model parameters from the literature. For all voxels with concordant positive and negative ΔBOLD, we observed a canonical hemodynamic response with average *n*-ratios of 2.0 and 1.6, respectively (Fig. 3d). Our data also confirm the presence of a substantial number of discordant voxels, comprising 31% of voxels with positive and 66% of voxels with negative ΔBOLD for CALC versus CTRL (Fig. 3c), and similarly for the REST (Supplementary Fig. 4a) and the MEM condition (Supplementary Fig. 4b). Additionally, we recalculated $\Delta CMRO_2$ via the Davis model using parameters (α, M) derived from our own data, yielding a similar percentage and regional distribution of discordant voxels, along with comparable $CMRO_2$ responses (Supplementary Fig. 7). In conclusion, these results strengthen the reliability of the mqBOLD approach, successfully validating the decades-old model parameters of the Davis model.

One could argue that discordant ΔBOLD arises from misalignment and partial volume effects when integrating voxel data across modalities. Thus, we performed a replication study with matched voxel sizes and matrices in BOLD and mqBOLD sequences, albeit sacrificing whole-brain coverage for higher voxel resolution in pCASL imaging. Utilizing the same study design and analysis pipeline of the main study, we again found an *n*-ratio > 1 for concordant voxels (BOLD pos/neg: 1.7/1.2) and, critically, a considerable proportion of discordant voxels (BOLD pos/neg: 40%/40%) (Supplementary Fig. 6). One may also discuss sensitivity issues of mqBOLD across cortical voxels. For instance, low pCASL sensitivity or high vascular effects (high R2′ or CBV) might lead to low ΔCBF and thus artificially induce discordant ΔBOLD. Consequently, we validated our results using control masks focusing on voxels with significant ΔCBF or $\Delta CMRO_2$, while excluding those with high vascular contributions (Supplementary Fig. 8). All control analyses confirmed the presence of discordant voxels, with both positive (11–29%) and negative (68–78%) ΔBOLD values. As a final control against voxel-specific artifacts, we investigated hemodynamic and metabolic responses for both signs of ΔBOLD within identical voxels (Fig. 4, conjunction mask). We assessed response patterns in approximately 4,000 voxels and classified them by response type. The 'concordant only' voxels displayed a canonical hemodynamic response for both positive and negative ΔBOLD (Fig. 4b(ii)), demonstrating that the mqBOLD method reliably detects canonical responses across the ΔBOLD spectrum. The largest group, labeled 'mixed' voxels, showed a canonical hemodynamic response for positive ΔBOLD (Fig. 4b(iii), red) but lacked a significant CBF response for negative ΔBOLD (Fig. 4b(iii), orange). Paradoxically, interpretation based solely on BOLD fMRI data would suggest increased activity in one condition and decreased in another, despite both tasks indicating a significant increase in $\Delta CMRO_2$ of similar magnitude in those voxels (Fig. 4b)(iii).

Discordant voxels occurred for both positive and negative ΔBOLD, as well as for $\Delta CMRO_2$ derived from Fick's formula and the Davis model. The presence of both concordant and discordant responses within identical voxels implies different hemodynamic mechanisms serving varying oxygen demands. Reference 31 identified microvascular variations between cortical and subcortical regions, and simultaneous recordings of neuronal activity and CBF suggest that interneuron activity may influence blood flow more than other neuronal activity[64–66]. In humans, refs. 16,67 both found discrepancies in the coupling of CBF and ΔBOLD in sensory cortices, which they interpreted as distinct neurovascular coupling mechanisms, particularly for negative ΔBOLD. In conclusion, mqBOLD effectively identifies canonical hemodynamic responses but also a considerable number of voxels exhibiting discordant ΔBOLD across various tasks and in relation to varying baseline conditions.

Baseline OEF predicts baseline metabolism and alternate hemodynamic coupling

According to Fick's principle, a change in $CMRO_2$ without CBF alteration arises from ΔOEF. We hypothesized that baseline OEF varies across voxels with different hemodynamic response types, suggesting the presence of regionally varying oxygen buffers. Our findings confirmed significantly different baseline OEFs across three response types among 'conjunction voxels' (Fig. 4c). Baseline OEF was lowest in 'discordant only' voxels and highest in 'concordant only' voxels, with 'mixed' voxels in between. We also observed a significant positive linear relationship between baseline $CMRO_2$, CBF and OEF across voxels of all tasks, covering more than 50% of all GM voxels (Fig. 5a(ii)). Multiple linear regression showed that OEF accounts for the majority of baseline $CMRO_2$ variability (>68%), followed by CBF (>28%) and CBV (>1%), which also aligned with QSM data[68,69] (Fig. 5c). Collectively, our results suggest that OEF is a key modulator of baseline metabolism across the human cortex, potentially predicting regional hemodynamic responses during tasks (Fig. 5d). In line with baseline results, multiple linear regression revealed that ΔOEF significantly contributes (58% of the total explained variance) to task-related oxygen demand in discordant voxels. Conversely, concordant voxels primarily accommodate $\Delta CMRO_2$ through ΔCBF (87%), supporting the canonical hemodynamic response. In summary, OEF is a strong predictor of baseline metabolism across the cortex, and ΔOEF regulates oxygen demand in spatially distributed voxels. Our findings align with rodent studies demonstrating varying neurovascular coupling based on variations in vascular composition[14,28,31].

Limitations of mqBOLD and control analyses

The mqBOLD method, although less invasive than PET, has notable limitations. Still, systematic biases in CBF, OEF and $CMRO_2$ quantification affect only across-subject comparisons and do not account for task effects, which are derived from ΔOEF or $\Delta CMRO_2$ within identical voxels.

Absolute quantification of CBV through dynamic susceptibility contrast (DSC) MRI is challenging, reflecting total rather than venous CBV. Yet this limitation applies to nearly all available CBV measurements, including PET[70]. To enhance intersubject comparability of CBV values, we implemented a global normalization procedure[44]. Despite these limitations, our CBV data are valuable as they represent a rare attempt to quantify baseline CBV and ΔCBV during task processing in healthy individuals.

We further evaluated the sensitivity of our mqBOLD method to accurately detect both positive and negative ΔCBF. Our analysis replicated the amplitude and extent of reduced CBF observed in a prior PET study (Supplementary Fig. 3b) using a similar analysis approach[71]. Additionally, our findings reveal ΔCBF in regions exhibiting significant positive ΔBOLD, aligning with earlier MRI-based CBF measurements[50,72].

Furthermore, $CMRO_2$ values in white matter (WM) are not interpretable because T2 and T2* quantification is influenced by orientation effects of myelinated nerve fibers and differences in lipid concentration between GM and WM. In prior work, our group addressed these systematic errors of background magnetic fields[44], T2-related bias[45] and orientation-related effects in WM structures[73]. Additionally, we used masking to reduce partial volume effects of adjacent WM structures, confirmed our main result in a replication study and demonstrated that mqBOLD-based OEF agreed well with PET-based OEF[46].

We also performed several control analyses to confirm the study design. A separate control study validated the stability of the BOLD (Supplementary Fig. 3d) and CBF (Supplementary Fig. 3e) signals during extended measurements. Crucially, neither signal exhibited habituation or drift effects during prolonged acquisition.

Future directions for BOLD fMRI

Our study reveals spatial variability in hemodynamic changes across the human cortex, suggesting diverse underlying mechanisms. First, voxels primarily governed by ΔOEF exhibit a greater oxygen buffer, maintaining adequate oxygen pressure during tasks[7,19]. Second, OEF regulation may indicate different signaling mechanisms[6], including astrocytic activity[74], shifts in excitatory/inhibitory signaling[75,76] or neuromodulatory regulation[77]. Third, our findings underscore the importance of quantitative mqBOLD fMRI for future research, particularly when examining groups with altered hemodynamics, such as in aging[30] or neurodegenerative conditions[78].

Online content

Any methods, additional references, Nature Portfolio reporting summaries, source data, extended data, supplementary information, acknowledgements, peer review information; details of author contributions and competing interests; and statements of data and code availability are available at https://doi.org/10.1038/s41593-025-02132-9.

References

1. Engl, E. & Attwell, D. Non-signalling energy use in the brain. *J. Physiol.* **593**, 3417–3429 (2015.
2. Kim, S.-G. & Ogawa, S. Biophysical and physiological origins of blood oxygenation level-dependent fMRI signals. *J. Cereb. Blood Flow Metab.* **32**, 1188–1206 (2012).
3. Attwell, D. et al. Glial and neuronal control of brain blood flow. *Nature* **468**, 232–243 (2010).
4. Drew, P. J. Vascular and neural basis of the BOLD signal. *Curr. Opin. Neurobiol.* **58**, 61–69 (2019).
5. Hillman, E. M. C. Coupling mechanism and significance of the BOLD signal: a status report. *Annu. Rev. Neurosci.* **37**, 161–181 (2014).
6. Howarth, C., Mishra, A. & Hall, C. N. More than just summed neuronal activity: how multiple cell types shape the BOLD response. *Phil. Trans. R. Soc. B* **376**, 20190630 (2020).
7. Leithner, C. & Royl, G. The oxygen paradox of neurovascular coupling. *J. Cereb. Blood Flow Metab.* **34**, 19–29 (2014).
8. Fox, P. T. & Raichle, M. E. Focal physiological uncoupling of cerebral blood flow and oxidative metabolism during somatosensory stimulation in human subjects. *Proc. Natl Acad. Sci. USA* **83**, 1140–1144 (1986).
9. Ances, B. M. et al. Regional differences in the coupling of cerebral blood flow and oxygen metabolism changes in response to activation: implications for BOLD-fMRI. *NeuroImage* **39**, 1510–1521 (2008).
10. Buxton, R. B. Interpreting oxygenation-based neuroimaging signals: the importance and the challenge of understanding brain oxygen metabolism. *Front. Neuroenergetics* https://doi.org/10.3389/fnene.2010.00008 (2010).
11. Devor, A. et al. Coupling of total hemoglobin concentration, oxygenation, and neural activity in rat somatosensory cortex. *Neuron* **39**, 353–359 (2003).
12. Gagnon, L. et al. Quantifying the microvascular origin of BOLD-fMRI from first principles with two-photon microscopy and an oxygen-sensitive nanoprobe. *J. Neurosci.* **35**, 3663–3675 (2015).
13. Logothetis, N. K., Pauls, J., Augath, M., Trinath, T. & Oeltermann, A. Neurophysiological investigation of the basis of the fMRI signal. *Nature* **412**, 150–157 (2001).
14. Boorman, L. et al. Negative blood oxygen level dependence in the rat: a model for investigating the role of suppression in neurovascular coupling. *J. Neurosci.* **30**, 4285–4294 (2010).
15. Devor, A. et al. Suppressed neuronal activity and concurrent arteriolar vasoconstriction may explain negative blood oxygenation level-dependent signal. *J. Neurosci.* **27**, 4452–4459 (2007).
16. Mullinger, K. J., Mayhew, S. D., Bagshaw, A. P., Bowtell, R. & Francis, S. T. Evidence that the negative BOLD response is neuronal in origin: a simultaneous EEG–BOLD–CBF study in humans. *NeuroImage* **94**, 263–274 (2014).
17. Shmuel, A., Augath, M., Oeltermann, A. & Logothetis, N. K. Negative functional MRI response correlates with decreases in neuronal activity in monkey visual area V1. *Nat. Neurosci.* **9**, 569–577 (2006).
18. Stefanovic, B., Warnking, J. M. & Pike, G. B. Hemodynamic and metabolic responses to neuronal inhibition. *NeuroImage* **22**, 771–778 (2004).
19. Leithner, C. et al. Pharmacological uncoupling of activation induced increases in CBF and $CMRO_2$. *J. Cereb. Blood Flow Metab.* **30**, 311–322 (2010).
20. Zaldivar, D., Rauch, A., Whittingstall, K., Logothetis, N. K. & Goense, J. Dopamine-induced dissociation of BOLD and neural activity in macaque visual cortex. *Curr. Biol.* **24**, 2805–2811 (2014).
21. Ekstrom, A. D. Regional variation in neurovascular coupling and why we still lack a Rosetta Stone. *Phil. Trans. R. Soc. B* **376**, 20190634 (2021).
22. Devor, A. et al. Stimulus-induced changes in blood flow and 2-deoxyglucose uptake dissociate in ipsilateral somatosensory cortex. *J. Neurosci.* **28**, 14347–14357 (2008).
23. Martínez-Maestro, M., Labadie, C. & Möller, H. E. Dynamic metabolic changes in human visual cortex in regions with positive and negative blood oxygenation level-dependent response. *J. Cereb. Blood Flow Metab.* **39**, 2295–2307 (2019).
24. Nagaoka, T. et al. Increases in oxygen consumption without cerebral blood volume change during visual stimulation under hypotension condition. *J. Cereb. Blood Flow Metab.* **26**, 1043–1051 (2006).

25. Stiernman, L. J. et al. Dissociations between glucose metabolism and blood oxygenation in the human default mode network revealed by simultaneous PET-fMRI. *Proc. Natl Acad. Sci. USA* **118**, e2021913118 (2021).
26. Buxton, R. B. & Frank, L. R. A model for the coupling between cerebral blood flow and oxygen metabolism during neural stimulation. *J. Cereb. Blood Flow Metab.* **17**, 64–72 (1997).
27. Cerri, D. H. et al. Distinct neurochemical influences on fMRI response polarity in the striatum. *Nat. Commun.* **15**, 1916 (2024).
28. Ekstrom, A. How and when the fMRI BOLD signal relates to underlying neural activity: the danger in dissociation. *Brain Res. Rev.* **62**, 233–244 (2010).
29. Sirotin, Y. B. & Das, A. Anticipatory haemodynamic signals in sensory cortex not predicted by local neuronal activity. *Nature* **457**, 475–479 (2009).
30. Tsvetanov, K. A., Henson, R. N. A. & Rowe, J. B. Separating vascular and neuronal effects of age on fMRI BOLD signals. *Phil. Trans. R. Soc. B* **376**, 20190631 (2021).
31. Shaw, K. et al. Neurovascular coupling and oxygenation are decreased in hippocampus compared to neocortex because of microvascular differences. *Nat. Commun.* **12**, 3190 (2021).
32. Devonshire, I. M. et al. Neurovascular coupling is brain region-dependent. *NeuroImage* **59**, 1997–2006 (2012).
33. Sanganahalli, B. G., Herman, P., Rothman, D. L., Blumenfeld, H. & Hyder, F. Metabolic demands of neural-hemodynamic associated and disassociated areas in brain. *J. Cereb. Blood Flow Metab.* **36**, 1695–1707 (2016).
34. Schridde, U. et al. Negative BOLD with large increases in neuronal activity. *Cereb. Cortex* **18**, 1814–1827 (2008).
35. Ito, H. et al. Integrated PET/MRI scanner with oxygen-15 labeled gases for quantification of cerebral blood flow, cerebral blood volume, cerebral oxygen extraction fraction and cerebral metabolic rate of oxygen. *Ann. Nucl. Med.* **35**, 421–428 (2021).
36. Alzaidi, A. A., Panek, R. & Blockley, N. P. Quantitative BOLD (qBOLD) imaging of oxygen metabolism and blood oxygenation in the human body: a scoping review. *Magn. Reson. Med.* **92**, 1822–1837 (2024).
37. Jiang, D. & Lu, H. Cerebral oxygen extraction fraction MRI: techniques and applications. *Magn. Reson. Med.* **88**, 575–600 (2022).
38. Wehrli, F. W. Recent advances in MR imaging-based quantification of brain oxygen metabolism. *Magn. Reson. Med. Sci.* **23**, 377–403 (2024).
39. Yablonskiy, D. A. & Haacke, E. M. Theory of NMR signal behavior in magnetically inhomogeneous tissues: the static dephasing regime. *Magn. Reson. Med.* **32**, 749–763 (1994).
40. He, X., Zhu, M. & Yablonskiy, D. A. Validation of oxygen extraction fraction measurement by qBOLD technique. *Magn. Reson. Med.* **60**, 882–888 (2008).
41. He, X. & Yablonskiy, D. A. Quantitative BOLD: Mapping of human cerebral deoxygenated blood volume and oxygen extraction fraction: default state. *Magn. Reson. Med.* **57**, 115–126 (2007).
42. Stone, A. J. & Blockley, N. P. A streamlined acquisition for mapping baseline brain oxygenation using quantitative BOLD. *NeuroImage* **147**, 79–88 (2017).
43. Christen, T., Schmiedeskamp, H., Straka, M., Bammer, R. & Zaharchuk, G. Measuring brain oxygenation in humans using a multiparametric quantitative blood oxygenation level dependent MRI approach. *Magn. Reson. Med.* **68**, 905–911 (2012).
44. Hirsch, N. M. et al. Technical considerations on the validity of blood oxygenation level-dependent-based MR assessment of vascular deoxygenation. *NMR Biomed.* **27**, 853–862 (2014).
45. Kaczmarz, S., Hyder, F. & Preibisch, C. Oxygen extraction fraction mapping with multi-parametric quantitative BOLD MRI: reduced transverse relaxation bias using 3D-GraSE imaging. *NeuroImage* **220**, 117095 (2020).
46. Kufer, J. et al. Imaging effective oxygen diffusivity in the human brain with multiparametric magnetic resonance imaging. *J. Cereb. Blood Flow Metab.* **42**, 349–363 (2022).
47. Wiestler, B. et al. Multiparametric MRI-based differentiation of WHO grade II/III glioma and WHO grade IV glioblastoma. *Sci. Rep.* **6**, 35142 (2016).
48. Davis, T. L., Kwong, K. K., Weisskoff, R. M. & Rosen, B. R. Calibrated functional MRI: mapping the dynamics of oxidative metabolism. *Proc. Natl Acad. Sci. USA* **95**, 1834–1839 (1998).
49. Fehr, T., Code, C. & Herrmann, M. Common brain regions underlying different arithmetic operations as revealed by conjunct fMRI–BOLD activation. *Brain Res.* **1172**, 93–102 (2007).
50. Lin, P., Hasson, U., Jovicich, J. & Robinson, S. A neuronal basis for task-negative responses in the human brain. *Cereb. Cortex* **21**, 821–830 (2011).
51. Raichle, M. E. et al. A default mode of brain function. *Proc. Natl Acad. Sci. USA* **98**, 676–682 (2001).
52. Andrews-Hanna, J. R., Saxe, R. & Yarkoni, T. Contributions of episodic retrieval and mentalizing to autobiographical thought: evidence from functional neuroimaging, resting-state connectivity, and fMRI meta-analyses. *NeuroImage* **91**, 324–335 (2014).
53. Spreng, R. N. & Grady, C. L. Patterns of brain activity supporting autobiographical memory, prospection, and theory of mind, and their relationship to the default mode network. *J. Cogn. Neurosci.* **22**, 1112–1123 (2010).
54. Addis, D. R., Wong, A. T. & Schacter, D. L. Remembering the past and imagining the future: common and distinct neural substrates during event construction and elaboration. *Neuropsychologia* **45**, 1363–1377 (2007).
55. DuPre, E., Luh, W.-M. & Spreng, R. N. Multi-echo fMRI replication sample of autobiographical memory, prospection and theory of mind reasoning tasks. *Sci. Data* **3**, 160116 (2016).
56. Anticevic, A. et al. The role of default network deactivation in cognition and disease. *Trends Cogn. Sci.* **16**, 584–592 (2012).
57. Cho, J. et al. Cerebral metabolic rate of oxygen ($CMRO_2$) mapping by combining quantitative susceptibility mapping (QSM) and quantitative blood oxygenation level-dependent imaging (qBOLD). *Magn. Reson. Med.* **80**, 1595–1604 (2018).
58. Gauthier, C. J., Desjardins-Crépeau, L., Madjar, C., Bherer, L. & Hoge, R. D. Absolute quantification of resting oxygen metabolism and metabolic reactivity during functional activation using QUO2 MRI. *NeuroImage* **63**, 1353–1363 (2012).
59. Zhang, J. et al. Quantitative mapping of cerebral metabolic rate of oxygen ($CMRO_2$) using quantitative susceptibility mapping (QSM): quantitative $CMRO_2$ mapping Using QSM. *Magn. Reson. Med.* **74**, 945–952 (2015).
60. Restom, K., Perthen, J. E. & Liu, T. T. Calibrated fMRI in the medial temporal lobe during a memory-encoding task. *NeuroImage* **40**, 1495–1502 (2008).
61. Zhang, Y. et al. Impaired cerebral vascular and metabolic responses to parametric N-back tasks in subjective cognitive decline. *J. Cereb. Blood Flow Metab.* **41**, 2743–2755 (2021).
62. DiNuzzo, M. et al. Neurovascular coupling is optimized to compensate for the increase in proton production from nonoxidative glycolysis and glycogenolysis during brain activation and maintain homeostasis of pH, $p\,CO_2$, and $p\,O_2$. *J. Neurochem.* **168**, 632–662 (2024).
63. Huo, B.-X., Smith, J. B. & Drew, P. J. Neurovascular coupling and decoupling in the cortex during voluntary locomotion. *J. Neurosci.* **34**, 10975–10981 (2014).
64. Anenberg, E., Chan, A. W., Xie, Y., LeDue, J. M. & Murphy, T. H. Optogenetic stimulation of GABA neurons can decrease local neuronal activity while increasing cortical blood flow. *J. Cereb. Blood Flow Metab.* **35**, 1579–1586 (2015).

65. Echagarruga, C. T., Gheres, K. W., Norwood, J. N. & Drew, P. J. nNOS-expressing interneurons control basal and behaviorally evoked arterial dilation in somatosensory cortex of mice. *eLife* **9**, e60533 (2020).
66. Nunez-Elizalde, A. O. et al. Neural correlates of blood flow measured by ultrasound. *Neuron* **110**, 1631–1640.e4 (2022).
67. Devi, R. et al. Multi-echo investigations of positive and negative CBF and concomitant BOLD changes. *NeuroImage* **263**, 119661 (2022).
68. Huck, J. et al. High resolution atlas of the venous brain vasculature from 7T quantitative susceptibility maps. *Brain Struct. Funct.* **224**, 2467–2485 (2019).
69. Lüsebrink, F. et al. Comprehensive ultrahigh resolution whole brain in vivo MRI dataset as a human phantom. *Sci. Data* **8**, 138 (2021).
70. Enmi, J. et al. Measurement of cerebral blood flow with dynamic susceptibility contrast MRI and comparison with O-15 positron emission tomography. *Int. Congr. Ser.* **1265**, 150–158 (2004).
71. Shulman, G. L. et al. Common blood flow changes across visual tasks: I. Increases in subcortical structures and cerebellum but not in nonvisual cortex. *J. Cogn. Neurosci.* **9**, 624–647 (1997).
72. Zou, Q., Gu, H., Wang, D. J., Gao, J. H. & Yang, Y. Quantification of load dependent brain activity in parametric N-back working memory tasks using pseudo-continuous arterial spin labeling (pCASL) perfusion imaging. *J. Cogn. Sci.* **12**, 129–149 (2011).
73. Kaczmarz, S., Göttler, J., Zimmer, C., Hyder, F. & Preibisch, C. Characterizing white matter fiber orientation effects on multi-parametric quantitative BOLD assessment of oxygen extraction fraction. *J. Cereb. Blood Flow Metab.* **40**, 760–774 (2020).
74. Takata, N. et al. Optogenetic astrocyte activation evokes BOLD fMRI response with oxygen consumption without neuronal activity modulation. *Glia* **66**, 2013–2023 (2018).
75. Buxton, R. B., Griffeth, V. E. M., Simon, A. B. & Moradi, F. Variability of the coupling of blood flow and oxygen metabolism responses in the brain: a problem for interpreting BOLD studies but potentially a new window on the underlying neural activity. *Front. Neurosci.* **8**, 139 (2014).
76. Uhlirova, H. et al. Cell type specificity of neurovascular coupling in cerebral cortex. *eLife* **5**, e14315 (2016).
77. Koush, Y. et al. Metabolic underpinnings of activated and deactivated cortical areas in human brain. *J. Cereb. Blood Flow Metab.* **41**, 986–1000 (2021).
78. Chen, J. J., Uthayakumar, B. & Hyder, F. Mapping oxidative metabolism in the human brain with calibrated fMRI in health and disease. *J. Cereb. Blood Flow Metab.* **42**, 1139–1162 (2022).
79. Thomas Yeo, B. T. et al. The organization of the human cerebral cortex estimated by intrinsic functional connectivity. *J. Neurophysiol.* **106**, 1125–1165 (2011).

Publisher's note Springer Nature remains neutral with regard to jurisdictional claims in published maps and institutional affiliations.

Open Access This article is licensed under a Creative Commons Attribution 4.0 International License, which permits use, sharing, adaptation, distribution and reproduction in any medium or format, as long as you give appropriate credit to the original author(s) and the source, provide a link to the Creative Commons licence, and indicate if changes were made. The images or other third party material in this article are included in the article's Creative Commons licence, unless indicated otherwise in a credit line to the material. If material is not included in the article's Creative Commons licence and your intended use is not permitted by statutory regulation or exceeds the permitted use, you will need to obtain permission directly from the copyright holder. To view a copy of this licence, visit http://creativecommons.org/licenses/by/4.0/.

© The Author(s) 2025

Methods

Participants

Main study. Forty-seven healthy adults were enrolled; 7 were excluded due to task difficulties ($n = 1$), contrast-agent issues ($n = 2$) or poor data quality ($n = 4$; for example, motion or susceptibility artifacts, unilateral CBF), leaving 40 right-handed participants (22 women, 18 men; mean age 32.1 ± 9.2 years) for analysis. Of these, 30 completed all four conditions (CALC, MEM, CTRL, REST), and 10 performed only CALC and CTRL but underwent two DSC scans, enabling within-subject ΔCBV estimation; analyses of MEM or REST thus includes 30 participants.

Control study. To assess BOLD fMRI stability during prolonged tasks, a separate cohort of 18 right-handed healthy adults (11 women, 7 men; mean age 28.1 ± 4.8 years) underwent BOLD fMRI.

Replication study. For a replication with harmonized voxel matrices and resolution across BOLD and mqBOLD sequences, ten healthy adults (five women, five men; mean age 31.8 ± 6.8 years) performed CALC and CTRL.

All participants gave written informed consent. Procedures were approved by the Ethics Review Board of the Klinikum Rechts der Isar, Technical University of Munich, and participants were compensated.

Task design

Participants were scanned supine, viewing instructions on a screen via a mirror mounted on the head coil. Right-hand responses were recorded with a button box (Cambridge Research Systems). Tasks were explained and briefly practiced before scanning, emphasizing accuracy over speed. All tasks were designed to maintain continuous engagement during BOLD and quantitative fMRI.

CALC (calculation task): This task aimed to elicit negative BOLD responses in the DMN and positive BOLD responses in task-positive networks. Participants solved arithmetic problems at their own pace, with a maximum response time of 10 s per task, following a design similar to that of ref. 50. Each trial presented a row of three numbers plus a question mark (n1, n2, n3,?) with instructions to solve the arithmetic and fill in the missing number. The solution followed this rule: n2 − n1 = DIFF, n2 = n1 + (1 × DIFF), n3 = n2 + (2 × DIFF) and ? = n3 + (3 × DIFF). For example, for the row 33 38 48?, DIFF = 5, making the correct answer 63. Participants selected from three response options, including the correct answer, each corresponding to a button on the response box.

MEM (autobiographical memory task): The MEM condition was based on the design of refs. 53,55, using cue words instead of pictures for consistency across tasks. Participants recalled a specific autobiographical event with as many details as possible, with the cue word displayed for up to 15 s. They pressed the first button twice upon recalling an event. If they couldn't recall any details, they pressed the second and third buttons in succession for a new cue word, ensuring uniformity in button presses across tasks.

CTRL (low-level baseline): The CTRL condition involved a simple task with minimal cognitive demands. A row of random letters was displayed for 5.9–8.9 s, and participants pressed a button to indicate whether the first letter was a vowel. This active baseline ensured visual input, and button presses were consistent with the CALC and MEM tasks.

REST (resting state baseline): Although studies on DMN activations typically use matched control tasks for contrasts[53–55], such as our CTRL condition, DMN deactivation studies often compare to an uncontrolled resting state baseline[50,51,56]. To replicate these DMN contrasts, we also collected REST data, featuring a white fixation cross on a black screen.

MRI acquisition parameters

Main study. MRI was conducted on a 3 T Philips Ingenia MRI scanner with an Elition upgrade and a 32-channel head coil. The quantitative fMRI protocol included multiparametric, quantitative BOLD (mqBOLD) and ASL imaging:

(1) Multiecho spin-echo T2 mapping: Three-dimensional (3D) gradient spin echo readout as implemented by our group[45] with 8 echoes of even-spaced echo times (TE): TE1 = ΔTE = 16 ms; TR = 251; readout duration = 128 ms; $\alpha = 90°$; voxel size $2 \times 2 \times 3.3$ mm^3; 35 slices (30 slices in 4 subjects); total acquisition time = 2:28 min (for 35 slices).

(2) Multiecho gradient-echo T2* mapping, as implemented by our group[44,45]: 12 echoes, TE1 = ΔTE = 5 ms; TR = 2,229 ms; readout duration = 60 ms; $\alpha = 30°$; voxel size $2 \times 2 \times 3$ mm^3; gap 0.3 mm; 35 slices (30 slices in 4 subjects). Correction for magnetic background gradients with a standard sinc-Gauss excitation pulse[80,81]; acquisition of half- and quarter-resolution data in k-space center for motion correction[82]; total acquisition time = 6:08 min (for 35 slices).

(3) DSC, as implemented by our group[83]: Single-shot GRE-EPI; echo planar imaging (EPI) factor 49; 80 dynamics; TR = 2.0 s; $\alpha = 60°$; acquisition voxel size $2 \times 2 \times 3.5$ mm^3; 35 slices (30 slices in 4 subjects). Injection of gadolinium-based contrast agent as a bolus after five dynamics, 0.1 ml kg^{-1}, minimum 6 ml, maximum 8 ml per injection, flow rate: 4 ml s^{-1}, additionally flushing with 25 ml NaCl; total acquisition time = 2:49 min (for 35 slices).

(4) Pseudocontinuous arterial spin labeling (pCASL): following ref. 84 and as implemented by our group[45,85]. Post-labeling delay 1,800 ms, label duration 1,800 ms; 4 background suppression pulses; two-dimensional EPI readout; TE = 11 ms; TR = 4,500 ms; $\alpha = 90°$; 20 slices (16 slices in 1 subject); EPI factor 29; acquisition voxel size $3.28 \times 3.5 \times 6.0$ mm^3; gap 0.6 mm; 39 dynamics plus one proton-density-weighted M0 scan; total acquisition time = 6:00 min.

In addition to quantitative fMRI, we acquired

(5) BOLD fMRI using single-shot EPI, EPI factor 43; voxel size = $3.0 \times 3.0 \times 3.0$ mm^3; FOV $192 \times 192 \times 127.8$ mm^3; TE = 30 ms; TR = 1.2 s; $\alpha = 70°$; 40 slices; SENSE-factor = 2; MB-SENSE-factor = 2; 400 dynamics (8:05 min) for 4 conditions, 200 dynamics (4:05 min) for 2 conditions, 1,650 dynamics (33:05 min) for the long-block control study acquisition. For susceptibility correction, a B_0 field map was acquired with two echoes; TR/TE1/TE2 = 525 ms/6.0 ms/9.8 ms; 40 slices; parallel acquisition; $\alpha = 60°$; voxel size = $3.0 \times 3.0 \times 3.0$ mm^3; FOV $192 \times 192 \times 127.8$ mm^3; total acquisition time = 0:35 s.

(6) T1-weighted 3D MPRAGE pre- and post-gadolinium (TI/TR/TE/α = 100 ms/9 ms/4 ms/8°; CS-SENSE-factor = 7.5; 170 slices; FOV = $240 \times 253 \times 170$ mm^3; voxel size $1.0 \times 1.0 \times 1.0$ mm^3; acquisition time = 2:05 min) and T2-weighted 3D fluid-attenuated inversion recovery (FLAIR) (TR/TE/α = 4,800/293/40°; CS-SENSE-factor = 10; 140 slices; FOV = $240 \times 248.9 \times 168$ mm^3; acquisition voxel size $1.2 \times 1.2 \times 1.2$ mm^3; turbo spin-echo factor 170; inversion delay 1,650 ms; acquisition time = 2:09 min) images were acquired for anatomical reference and to exclude brain lesions.

Control study. MRI was performed on a 3 T Philips Ingenia scanner with a 32-channel head coil and included only T1-weighted 3D MPRAGE and BOLD fMRI, with all acquisition parameters being identical to those described above.

Replication study. MRI was performed identical to the main study, but with matching voxel matrices: T1-weighted 3D MPRAGE, multiecho spin-echo T2 mapping and multiecho gradient-echo T2* mapping as described above, with T2/T2* voxel size = $2 \times 2 \times 3.0$ mm^3, gap 0.3 mm. BOLD fMRI as described above, but with a voxel acquisition size = $4 \times 4 \times 3$ mm^3, gap 0.3 mm, 40 slices. pCASL as described above,

with BOLD fMRI voxel size ($4 \times 4 \times 3$ mm^3, gap 0.3 mm; 26 slices). As a result, subject data were acquired with harmonized voxel dimensions: that is, matching BOLD and pCASL voxel sizes and four T2/T2* voxels per BOLD/pCASL voxels in the x–y plane. Whole-brain coverage was not possible with this higher-resolution pCASL sequence; thus, we positioned the volume at the same angle as before to cover all key regions of interest (ROIs) from our main study ('brain coverage', Supplementary Fig. 6).

Data acquisition

After obtaining informed written consent, a physician placed a venous catheter for blood sampling (hemoglobin, hematocrit (Hct), creatinine). DSC contrast was administered only if creatinine was normal, ensuring renal health. Arterial oxygen saturation was tracked via pulse oximetry (Nonin Medical B.V.).

Main study. Figure 1b illustrates the imaging session from the main study.

BOLD fMRI: The four task conditions were presented using a 30-second block design, each repeated four times in random order. BOLD alternated with mqBOLD fMRI runs to reduce habituation or fatigue effects. During mqBOLD imaging, conditions were presented pseudo-randomly for pCASL and T2* mapping. DSC (CTRL) were performed at the end of the session to avoid signal artifacts. The contrast agent was administered via a pump (Medtron AG) under a medical doctor's supervision.

After the imaging session, participants completed a memory questionnaire about the MEM condition, rating the ease of recalling specific events on a difficulty scale (1 = 'very easy' to 4 = 'very difficult') and the detail of their memories on a concreteness scale (1 = 'very detailed' to 4 = 'very vague'). On average, participants scored 1.8 ± 0.7 on difficulty and 2.0 ± 0.6 on concreteness, indicating that recalling events was relatively easy and memories were reasonably detailed. Participants took an average of only 2.5 ± 1 s to recall an event.

A subsample of $N = 10$ subjects from the main study performed only the CALC and CTRL conditions but instead received two DSC scans (totaling a full clinical dose of 16 ml). This enabled calculation of within-subject ΔCBV for task effects.

Control study. fMRI BOLD data were obtained for CALC and MEM tasks with a 30-s block design (four repetitions each, interleaved with 30-s CTRL blocks), alongside extended 3-min blocks (four repetitions each, interleaved with 1-min CTRL blocks), totaling 41 min of scan time.

Replication study. Study design and data acquisition were identical to the main study, utilizing the group median CBV data from the main study for analyses.

Image processing

Processing of BOLD fMRI data. BOLD fMRI data were preprocessed using fMRIPrep 20.2.4 (ref. 86) within a Docker container based on Nipype 1.6.1 (ref. 87). Preprocessing involved segmentation, estimation of motion parameters and other confounds, correction for susceptibility distortions, coregistration in native T1w space and normalization to MNI152-ICBM-2mm space with a nonlinear sixth-generation registration model developed by Montreal Neurological Institute, McGill University. fMRIPrep relies on FSL 5.0.9 for registering EPI time-series data to T1w data with boundary-based registration, FSL FAST for brain tissue segmentation and ANTs 2.3.3 (ref. 88) for spatial normalization to MNI space in a multiscale, mutual-information-based, nonlinear registration scheme, where all transforms are first concatenated and registration steps applied at once. As part of the fMRIPrep pipeline[89,90], correction for head motion and susceptibility distortions was performed in the subject's native space, applying a single composite transform to the BOLD fMRI time series. The same data were also resampled into standard space, generating a preprocessed BOLD run in MNI152NLin6Asym space. Preprocessed BOLD fMRI data, without global signal regression, were then used as input to the PLS model. All datasets from the main, control and replication studies underwent identical processing.

Calculation of quantitative parameter maps from mqBOLD data. We calculated quantitative parameter maps using in-house scripts (in Matlab) and SPM12 (Wellcome Trust Centre for Neuroimaging, UCL). Figure 1 illustrates the procedure and shows representative subject-averaged parameter maps.

T2/T2*-mapping: Quantitative T2 and T2* parameter maps were obtained by applying monoexponential fits to multiecho spin and gradient echo data, as described by our group[44,45,91]. Corrections for macroscopic magnetic background fields were implemented[81], and motion artifacts were addressed through redundant acquisitions of k-space centers[82].

R2′ maps were calculated via

$$R2' = \frac{1}{T2^*} - \frac{1}{T2} \quad (1)$$

yielding the transverse, reversible relaxation rate that depends on the vascular dHb content within a voxel[92,93]. Caution is required when interpreting these values at air–tissue boundaries (magnetic field inhomogeneities), in deep GM (iron deposition) or in WM structures (orientation effects in myelin), as previously discussed[45,81].

CBV maps were derived from DSC MRI after contrast agent application via integration of leakage-corrected ΔR2* curves[94] and subsequent normalization to a WM value of 2.5% (ref. 95). The DSC procedure has been described by our group[83,96].

OEF maps were calculated from R2′ and CBV parameter maps via the mqBOLD approach[39,43] and, as implemented by our group[44], via

$$OEF = \frac{R2'}{c \times sCBV} \quad (2)$$

with $c = \gamma \times \frac{4}{3} \times \pi \times \Delta\chi_0 \times Hct \times B_0$ (gyromagnetic ratio $\gamma = 2.675 \times 10^8\ s^{-1}\ T^{-1}$; susceptibility difference between fully deoxygenated and oxygenated hemoglobin $\Delta\chi_0 = 0.264 \times 10^{-6}$; magnetic field strength $B_0 = 3$ T; small-vessel hematocrit Hct, calculated as 85% of the (large-vessel) hematocrit values measured in each subject[44,97]). OEF (ratio) represents the amount of oxygen extracted from capillaries among passage.

CBF maps were calculated from pCASL data as described in ref. 84. Specifically, CBF was calculated as the pairwise difference of the averaged and motion-corrected label and control images and then scaled by a proton-density-weighted image.

$CMRO_2$ maps: For each condition separately, we calculated the voxel-wise $CMRO_2$ by combining all parameter maps via Fick's principle:

$$CMRO_2 = OEF \times CBF \times C_aO_2 \quad (3)$$

where C_aO_2 reflects the arterial oxygen content (in µmol) for each subject and was calculated as $C_aO_2 = 0.334 \times Hct \times 55.6 \times O_2sat$, with O_2sat being the oxygen saturation measured by a pulse oximeter[93].

All parameter maps were calculated in subject space and coregistered to the first echo of the T2 data. Any normalization into MNI space was performed afterward. Specifically, parameter maps were first coregistered to native T1w space before applying the normalization matrix to MNI space, as derived from fMRIPrep. CBF values were upscaled by 25% to account for the systematic underestimation of CBF due to the four background suppression pulses, as motivated here[98,99]. The data of the replication study were processed identically to those of the main study.

Artifact correction and GM masking. For our analyses in standard space, we excluded voxels that fell within the lowest 15th percentile of the temporal SNR for more than 66% of participants, based on the BOLD fMRI data from each subject and voxel. The excluded voxels were primarily found in regions with significant susceptibility artifacts, such as the fronto- and temporo-basal brain areas. Additionally, we masked out the cerebellum and any voxels with a GM probability of less than 0.5. The resulting group mask was then applied to both the output of the GLM group analysis and the input matrices for the PLS analyses. For the analyses in native space, we additionally masked CSF-prone areas (T2 > 90 ms), high-susceptibility areas ($R2' > 9\ s^{-1}$), voxels with a high percentage of blood volume (CBV > 10%, probably driven by larger veins/arteries) and voxels with biologically implausible values, such as T2′ > 90 ms, OEF > 0.9 and CBF > 90 milliliters per 100 grams per minute.

Estimation of a realistic surrogate for CBV during CALC. After a sensitivity analysis at our institution, we found that half the clinical dosage of contrast agent was sufficient to reliably assess CBV in healthy subjects. Therefore, the final subset of ten participants received two half-dosages during the CALC and CTRL conditions, allowing us to quantify CBV in both conditions. We calculated the voxel ΔCBV for CALC compared to CTRL in subject space and averaged the results across Glasser's 360 functional ROIs[100]. This subject-averaged ΔCBV map was then used to estimate a CBV surrogate map for the remaining 30 subjects, who had only one baseline CBV measurement. These data are among the most empirically supported data for ΔCBV in quantitative fMRI studies, but this was possible only for the CALC condition. Hence, we continued using the CBV CTRL map to calculate $CMRO_2$ during the MEM condition.

Semiquantitative, BOLD-informed, $CMRO_2$ estimation. The estimation of quantitative $CMRO_2$ maps relies on the combination of R2′, CBV and CBF values, according to equation (3). To control for potential error propagation during voxel-wise analyses, especially from R2′ measurements (see appendix in ref. 73), we calculated R2′ parameter maps during MEM and CALC from baseline R2′ and BOLD fMRI data as suggested by ref. 101. Instead of calculating ΔR2′ from quantitative R2′ (multiecho gradient-echo-based T2*) during task conditions, ΔR2′ is approximated as

$$\Delta R2' = -\frac{\Delta S}{S_0}\frac{1}{TE \times R2'_0} \quad (4)$$

with TE = 30 ms, $R2'_0$ being the baseline R2′ and $\frac{\Delta S}{S_0}$ the BOLD signal change, derived from task data. R2′ in CALC and MEM was calculated via $R2' = R2'_0 + (\Delta R2' \times R2'_0)$ and fed into OEF and $CMRO_2$ calculations according to equations (2) and (3). These semiquantitative $CMRO_2$ parameter maps differ from the regional $CMRO_2$ maps only in their underlying R2′ values. In Supplementary Fig. 5, we compared the PLS results of the BOLD-informed approach with those of the fully quantitative approach and found very similar signal ranges and voxel distributions.

Davis model. The Davis model was originally designed for calibrated fMRI and allows to derive $\Delta CMRO_2$ by using carbon dioxide breathing as a physiological method to manipulate CBF independently of $CMRO_2$. The model relies on the parameters M, α and β (ref. 48):

$$\frac{\Delta S}{S_0} = M\left[1 - \left(\frac{CBF}{CBF_0}\right)^{\alpha-\beta}\left(\frac{CMRO_2}{CMRO_{2,0}}\right)^{\beta}\right] \quad (5)$$

where α is a power-law exponent relating ΔCBV to ΔCBF, β reflects the microvascular anatomy[93] and M is commonly referred to the maximum ΔBOLD that occurs when all hemoglobin is fully oxygenated and depends on baseline OEF[92]. Previously, $\alpha = 0.38$ was used[102], but more recent studies have identified lower values. In Fig. 3a, we plotted the range of predicted ΔBOLD using empirical values for all parameters, derived from recent calibration studies with $\alpha = 0.23$, $\beta = 1.3$ (ref. 93) and $M = 5.5$ (ref. 78). Assuming α and β, the fractional change in $CMRO_2$ can be calculated from combined BOLD signal and CBF measurements during tasks[78,92,103].

Statistics

PLS analysis of BOLD and mqBOLD data. PLS analyses were performed using the pyls library in the Python language (Python Software Foundation, version 3.8). Mean-centered PLS is a data-reduction method that computes latent variables (LVs) and corresponding brain patterns, optimizing the relationship between brain signals and experimental design[104]. In this study, we used PLS analyses to perform group-level statistics to identify brain regions that distinguish between task conditions (CALC or MEM) and a baseline condition (CTRL or REST). This analysis was applied to both BOLD fMRI and mqBOLD data, allowing for comparison of statistical maps. For mqBOLD data, we used quantitative OEF, CBF or $CMRO_2$ values per voxel and subject. For BOLD fMRI data, we used median percent signal change (from either CTRL or REST) across 24 s (20 TRs) per task condition, excluding the first 6 s of each task block to account for the hemodynamic response lag.

The significance of the LVs (multivariate patterns) was tested using permutation tests (3,000 permutations), and the reliability of brain saliences (voxel contributions) was assessed through bootstrap resampling (3,000 samples). Significant brain regions were identified using the bootstrap ratio (BSR), where a BSR > ±2 suggests a 95% confidence interval (CI) if the bootstrap distribution is normal[105,106]. To interpret BSR maps, they must be compared to design scores of each condition within each LV for task differences. In this manuscript, orange-red indicates a positive task effect (higher values during the task versus baseline), and blue indicates the opposite. We visualized the whole-brain, non-thresholded PLS results by transforming statistical maps from native to surface space with the 'vol_to_surf' function from nilearn's surface toolbox and plotted them on the 'fsaverage pial left and right mesh' using 'plot_surf_stat_mat.'

BOLD clusters. The BOLD clusters in Fig. 2d are based on a PLS analysis of BOLD data, with statistical maps thresholded at a BSR score of >±3. We extracted regions with a size of >1,000 connected voxels using Nilearn's region package in Python and fused fragmented clusters that belonged to the same Yeo network upon visual inspection[79].

General linear modeling of BOLD data. To validate the PLS analyses, we used a general linear model (GLM) approach as recommended by ref. 107. The GLM included confound variables such as CSF and WM signals, dvars, framewise displacement and translations/rotations across the x, y and z axes. We applied a high-pass filter (100 s) and a 6-mm smoothing kernel. For native space analyses, we used individual first-level z maps ($z > 2.5$). The contrasts calculated were CALC-positive (CALC > CTRL or REST), CALC-negative (CALC < CTRL or REST), MEM-positive (MEM > CTRL) and MEM-negative (MEM < CTRL). To cross-validate the PLS results, we used FWE-corrected z maps from the second-level analysis.

Other statistical analyses. For the native space analyses, we calculated median values within each native-space ROI from the first-level GLM output ($z > 2.5$) for each subject. We assessed significant task-related differences compared to baseline using paired-samples two-sided t-tests across subjects. For other analyses, we obtained median voxel values in standard space across subjects (Figs. 2b, 3b and 4a,d). Bar plots (Fig. 2d) were created using Python's seaborn library[108] with error bars indicating a 95% CI based on 2,000 bootstraps. A CI that included zero indicated a statistically nonsignificant median delta value.

To analyze hemodynamic differences between discordant and concordant voxels, we conducted paired *t*-tests on median subject values, and baseline differences were assessed using independent-sample permutation tests. High-resolution external maps were downsampled to 2-mm MNI standard space before analysis.

Reporting summary

Further information on research design is available in the Nature Portfolio Reporting Summary linked to this article.

Data availability

All raw and processed data are publicly available on OpenNEURO at https://openneuro.org/datasets/ds004873 (ref. 109).

Code availability

The scripts and Python Jupyter notebooks for quantitative parameter map analyses and the configuration files for replication of all analyses and figures are available on GitHub at https://github.com/NeuroenergeticsLab/two_modes_of_hemodynamics. The scripts for generating the parameter maps are available on GitHub at https://gitlab.lrz.de/nmrm_lab/public_projects/mq-bold.

References

80. Baudrexel, S. et al. Rapid single-scan *T* -mapping using exponential excitation pulses and image-based correction for linear background gradients. *Magn. Reson. Med.* **62**, 263–268 (2009).
81. Hirsch, N. M. & Preibisch, C. T2* mapping with background gradient correction using different excitation pulse shapes. *Am. J. Neuroradiol.* **34**, E65–E68 (2013).
82. Nöth, U., Volz, S., Hattingen, E. & Deichmann, R. An improved method for retrospective motion correction in quantitative T2* mapping. *NeuroImage* **92**, 106–119 (2014).
83. Hedderich, D. et al. Consistency of normalized cerebral blood volume values in glioblastoma using different leakage correction algorithms on dynamic susceptibility contrast magnetic resonance imaging data without and with preload. *J. Neuroradiol.* **46**, 44–51 (2019).
84. Alsop, D. C. et al. Recommended implementation of arterial spin-labeled perfusion MRI for clinical applications: a consensus of the ISMRM perfusion study group and the European consortium for ASL in dementia. *Magn. Reson. Med.* **73**, 102–116 (2015).
85. Göttler, J. et al. Flow-metabolism uncoupling in patients with asymptomatic unilateral carotid artery stenosis assessed by multi-modal magnetic resonance imaging. *J. Cereb. Blood Flow Metab.* **39**, 2132–2143 (2019).
86. Esteban, O. et al. fMRIPrep: a robust preprocessing pipeline for functional MRI. *Nat. Methods* **16**, 111–116 (2019).
87. Gorgolewski, K. et al. Nipype: a flexible, lightweight and extensible neuroimaging data processing framework in Python. *Front. Neuroinform* **5**, 13 (2011).
88. Avants, B., Epstein, C., Grossman, M. & Gee, J. Symmetric diffeomorphic image registration with cross-correlation: evaluating automated labeling of elderly and neurodegenerative brain. *Med. Image Anal.* **12**, 26–41 (2008).
89. Jenkinson, M., Beckmann, C. F., Behrens, T. E. J., Woolrich, M. W. & Smith, S. M. FSL. *NeuroImage* **62**, 782–790 (2012).
90. Smith, S. M. et al. Advances in functional and structural MR image analysis and implementation as FSL. *NeuroImage* **23**, S208–S219 (2004).
91. Preibisch, C., Volz, S., Anti, S. & Deichmann, R. Exponential excitation pulses for improved water content mapping in the presence of background gradients. *Magn. Reson. Med.* **60**, 908–916 (2008).
92. Blockley, N. P., Griffeth, V. E. M., Simon, A. B. & Buxton, R. B. A review of calibrated blood oxygenation level-dependent (BOLD) methods for the measurement of task-induced changes in brain oxygen metabolism. *NMR Biomed.* **26**, 987–1003 (2013).
93. Bright, M. G., Croal, P. L., Blockley, N. P. & Bulte, D. P. Multiparametric measurement of cerebral physiology using calibrated fMRI. *NeuroImage* **187**, 128–144 (2019).
94. Boxermann, J. L., Schmainda, K. M. & Weisskoff, R. M. Relative cerebral blood volume maps corrected for contrast agent extravasation significantly correlate with glioma tumor grade, whereas uncorrected maps do not. *Am. J. Neuroradiol.* **27**, 859–867 (2006).
95. Leenders, K. L. et al. Cerebral blood flow, blood volume and oxygen utilization: normal values and effect of age. *Brain* **113**, 27–47 (1990).
96. Kluge, A. et al. Analysis of three leakage-correction methods for DSC-based measurement of relative cerebral blood volume with respect to heterogeneity in human gliomas. *Magn. Reson. Imaging* **34**, 410–421 (2016).
97. Eichling, J. O., Raichle, M. E., Grubb, R. L., Larson, K. B. & Ter-Pogossian, M. M. In vivo determination of cerebral blood volume with radioactive oxygen-15 in the monkey. *Circ. Res.* **37**, 707–714 (1975).
98. Garcia, D. M., Duhamel, G. & Alsop, D. C. Efficiency of inversion pulses for background suppressed arterial spin labeling. *Magn. Reson. Med.* **54**, 366–372 (2005).
99. Mutsaerts, H. J. M. M. et al. Inter-vendor reproducibility of pseudo-continuous arterial spin labeling at 3 tesla. *PLoS ONE* **9**, e104108 (2014).
100. Glasser, M. F. et al. A multi-modal parcellation of human cerebral cortex. *Nature* **536**, 171–178 (2016).
101. Fujita, N., Matsumoto, K., Tanaka, H., Watanabe, Y. & Murase, K. Quantitative study of changes in oxidative metabolism during visual stimulation using absolute relaxation rates. *NMR Biomed.* **19**, 60–68 (2006).
102. Grubb, R. L., Raichle, M. E., Eichling, J. O. & Ter-Pogossian, M. M. The effects of changes in Pa CO_2 cerebral blood volume, blood flow, and vascular mean transit time. *Stroke* **5**, 630–639 (1974).
103. Germuska, M. & Wise, R. G. Calibrated fMRI for mapping absolute CMRO2: practicalities and prospects. *NeuroImage* **187**, 145–153 (2019).
104. McIntosh, A. R. & Lobaugh, N. J. Partial least squares analysis of neuroimaging data: applications and advances. *NeuroImage* **23**, S250–S263 (2004).
105. Krishnan, A., Williams, L. J., McIntosh, A. R. & Abdi, H. Partial least squares (PLS) methods for neuroimaging: a tutorial and review. *NeuroImage* **56**, 455–475 (2011).
106. McIntosh, A. R. & Mišić, B. Multivariate statistical analyses for neuroimaging data. *Annu. Rev. Psychol.* **64**, 499–525 (2013).
107. Esteban, O. et al. Analysis of task-based functional MRI data preprocessed with fMRIPrep. *Nat. Protoc.* **15**, 2186–2202 (2020).
108. Waskom, M. seaborn: statistical data visualization. *J. Open Source Softw.* **6**, 3021 (2021).
109. Epp, S. et al. Two distinct modes of hemodynamic responses in the human brain. *OpenNeuro* https://doi.org/10.18112/openneuro.ds004873.v2.0.6 (2025).

Acknowledgements

We thank A. Bose, A. Hechler, M. Ashrafi, R. Belenya, L. Fraticelli, S. Kaczmarz, J. Kufer and G. Hoffmann for their methodological support, discussions and suggestions on this work, and C. Zimmer for his overall support of the study. V.R. acknowledges support from the European Research Council (ERC) under the European Union's Horizon 2020 research and innovation program (ERC Starting Grant, grant no. 759659). C.P. has been funded by the Deutsche Forschungsgemeinschaft (DFG, German Research Foundation, grant no. 395030489).

Author contributions

S.M.E. designed the study, acquired the data, performed all analyses and wrote the manuscript. G.C. assisted with data analyses. B.Y. performed Davis model analysis. J.A.-H. designed the study. C.P. designed the study and developed the mqBOLD analysis pipeline. V.R. designed the study, supervised the project and wrote the manuscript.

Funding

Open access funding provided by Friedrich-Alexander-Universität Erlangen-Nürnberg.

Competing interests

The authors declare no competing interests.

Additional information

Supplementary information The online version contains supplementary material available at https://doi.org/10.1038/s41593-025-02132-9.

Correspondence and requests for materials should be addressed to Valentin Riedl.

Peer review information *Nature Neuroscience* thanks Oscar Esteban, Harald Möller and the other, anonymous, reviewer(s) for their contribution to the peer review of this work.

Reprints and permissions information is available at www.nature.com/reprints.

nature portfolio

Corresponding author(s): Valentin Riedl

Last updated by author(s): October 7, 2025

Reporting Summary

Nature Portfolio wishes to improve the reproducibility of the work that we publish. This form provides structure for consistency and transparency in reporting. For further information on Nature Portfolio policies, see our Editorial Policies and the Editorial Policy Checklist.

Statistics

For all statistical analyses, confirm that the following items are present in the figure legend, table legend, main text, or Methods section.

n/a	Confirmed
☐	☒ The exact sample size (*n*) for each experimental group/condition, given as a discrete number and unit of measurement
☐	☒ A statement on whether measurements were taken from distinct samples or whether the same sample was measured repeatedly
☐	☒ The statistical test(s) used AND whether they are one- or two-sided *Only common tests should be described solely by name; describe more complex techniques in the Methods section.*
☐	☒ A description of all covariates tested
☐	☒ A description of any assumptions or corrections, such as tests of normality and adjustment for multiple comparisons
☐	☒ A full description of the statistical parameters including central tendency (e.g. means) or other basic estimates (e.g. regression coefficient) AND variation (e.g. standard deviation) or associated estimates of uncertainty (e.g. confidence intervals)
☐	☒ For null hypothesis testing, the test statistic (e.g. *F*, *t*, *r*) with confidence intervals, effect sizes, degrees of freedom and *P* value noted *Give P values as exact values whenever suitable.*
☒	☐ For Bayesian analysis, information on the choice of priors and Markov chain Monte Carlo settings
☒	☐ For hierarchical and complex designs, identification of the appropriate level for tests and full reporting of outcomes
☐	☒ Estimates of effect sizes (e.g. Cohen's *d*, Pearson's *r*), indicating how they were calculated

Our web collection on statistics for biologists contains articles on many of the points above.

Software and code

Policy information about availability of computer code

Data collection	Main study: 3T Philips Elition Ingenia MR scanner (Philips Healthcare, Best, The Netherlands). Control study: 3T Philips Ingenia MR scanner (Philips Healthcare, Best, The Netherlands). Replication study: 3T Philips Elition Ingenia MR scanner (Philips Healthcare, Best, The Netherlands).
Data analysis	The calculation of the quantitative parameter maps was performed with in-house scripts in Matlab and SPM12 (Wellcome Trust Centre for Neuroimaging, UCL, London, UK), scripts can be downloaded here: https://gitlab.lrz.de/nmrm_lab/public_projects/mq-bold. The BOLD fMRI localizer data were pre-processed using fMRIPrep 20.2.4 in a docker container, which is based on Nipype 1.6.1. FMRIPrep relies on FSL 5.0.9 and ANTs 2.3.3. The subsequent data analyses and processing was performed using Python (version 3.8) and the following packages: Pandas (version 1.5.2), Numpy (version 1.23.5) and SciPy (version 1.9.3); the neuroimaging data were handled using Nilearn (version 0.9.2 and Nibabel (version 4.0.2); the plotting was performed with Matplotlib and (version 3.6.2, Seaborn (version 0.12.1). Cluster analysis was performed via atlasreader (version 0.1.2) and partial least squares analyses via pyls (version 0.1.6), permutation testing and t-test via scipy (version 1.9.3). Regression models were calculated via pingouin (version 0.5.4) and statsmodels (version 0.14.1). T The scripts (Python Jupyter notebooks) for replication of all analyses and figures are available on GitHub (https://github.com/NeuroenergeticsLab/two_modes_of_hemodynamics).

For manuscripts utilizing custom algorithms or software that are central to the research but not yet described in published literature, software must be made available to editors and reviewers. We strongly encourage code deposition in a community repository (e.g. GitHub). See the Nature Portfolio guidelines for submitting code & software for further information.

Data

Policy information about availability of data

All manuscripts must include a data availability statement. This statement should provide the following information, where applicable:

- Accession codes, unique identifiers, or web links for publicly available datasets
- A description of any restrictions on data availability
- For clinical datasets or third party data, please ensure that the statement adheres to our policy

All raw and processed data are available in the online repository of OpenNeuro (Epp et al., 2023) (https://openneuro.org/datasets/ds004873).

Research involving human participants, their data, or biological material

Policy information about studies with human participants or human data. See also policy information about sex, gender (identity/presentation), and sexual orientation and race, ethnicity and racism.

Reporting on sex and gender	The sex of the participants was self-reported. 22 women and 18 men were included in the main study cohort (N=40), 11 women and 7 men were included in the control study cohort and 5 men and 5 women were included in the replication study. We did not perform separated sex-based analyses as the ratio in the main cohort was well-balanced.
Reporting on race, ethnicity, or other socially relevant groupings	We did not include reportings of race, ethnicity or other socially relevant groupings in our analyses.
Population characteristics	Three cohorts of self-reported right-handed healthy participants were analyzed. Main study cohort: 40 participants, 22 female, 18 male, mean age 32.1 ± 9.2y. Control study cohort: 18 participants, 11 female, 7 male, mean age 28.1 ± 4.8y. Replication study cohort: 10 participants, 5 female, 5 male, mean age 31.8 ± 6.8y.
Recruitment	The participants were recruited word-of-mouth and using advertisement in the newsletter from hospital and university.
Ethics oversight	Participants were informed about the objectives and potential risks of the study, and signed a written consent form. The study was approved by the local institutional review board of the Klinikum rechts der Isar (382/18S) and was conducted in accordance with the Declaration of Helsinki.

Note that full information on the approval of the study protocol must also be provided in the manuscript.

Field-specific reporting

Please select the one below that is the best fit for your research. If you are not sure, read the appropriate sections before making your selection.

☒ Life sciences ☐ Behavioural & social sciences ☐ Ecological, evolutionary & environmental sciences

For a reference copy of the document with all sections, see nature.com/documents/nr-reporting-summary-flat.pdf

Life sciences study design

All studies must disclose on these points even when the disclosure is negative.

Sample size	The sample size of healthy participants for the main study (47 subjects acquired, 40 included in the analyses) was not predetermined, as we did not find previous studies employing a cognitive design looking at ΔCMRO2. However, in a pilot study (Epp et al., OHBM poster 2019), we did find significant metabolic activation in visual cortex using visual checkerboard stimulation and mqBOLD imaging with N=12 sample size, which made us confident to identify activations in higher-order cortices with more complex designs in N=40.
Data exclusions	Seven datasets (out of 47) had to be excluded because of a) apparent behavioral task difficulties (n=1), b) problems with contrast-agent application (n=2), or c) data quality problems (severe motion artifacts in CBF or R2' data, unilateral CBF data in one condition, huge susceptibility artifacts) (n=4).
Replication	Prior to uploading our scripts on Github we cleaned all scripts and replicated all analyses and results. Further, to undermine our findings, we acquired a replication dataset with 10 subjects, employing an adjusted voxel resolution in the fMRI BOLD and BOLD ASL sequences.
Randomization	Participants were not divided into groups, so no randomization was necessary. Task conditions were displayed in a pseudo-random order, so that for every participant, every condition preceeded every other condition at least once. The fMRI BOLD task localizer was run in the beginning of the experiment for 23 subject, and at the end of the experiment for the other 17 subjects, to account for possible habituation effects that impact the BOLD-signal amplitude.
Blinding	Blinding was not relevant for this study as participants were not divided into groups.

Reporting for specific materials, systems and methods

We require information from authors about some types of materials, experimental systems and methods used in many studies. Here, indicate whether each material, system or method listed is relevant to your study. If you are not sure if a list item applies to your research, read the appropriate section before selecting a response.

Materials & experimental systems

n/a	Involved in the study
☒	☐ Antibodies
☒	☐ Eukaryotic cell lines
☒	☐ Palaeontology and archaeology
☒	☐ Animals and other organisms
☒	☐ Clinical data
☒	☐ Dual use research of concern
☒	☐ Plants

Methods

n/a	Involved in the study
☒	☐ ChIP-seq
☒	☐ Flow cytometry
☐	☒ MRI-based neuroimaging

Plants

Seed stocks: n/a

Novel plant genotypes: n/a

Authentication: n/a

Magnetic resonance imaging

Experimental design

Design type: Cognitive task design. fMRI BOLD: block design.

Design specifications: fMRI BOLD: 30s blocks, 4 repetitions per condition. Quantitative fMRI measurements: one condition per sequence, sequence durations of approx. 6min.

Behavioral performance measures: Button presses were collected during task performance in the scanner. Reaction times were analyzed for the calculation, the memory and the control conditions. Correct responses were analyzed for the calculation task and the control task.
To assess the validity of the memory condition, during a 15-25min break after the quantitative measurements, the 30 participants who underwent all four conditions additionally completed a memory questionnaire, where they had to indicate how easy they found it to remember concrete events (difficulty scale; 1='very easy', 2='rather easy', 3='rather difficult', 4='very difficult') and how detailed their memories were overall (concreteness scale; 1='very detailed', 2='rather detailed', 3='rather vague', 4='very vague'). On average, people scored 1.8 +/- 0.7 (mean +/- standard deviation) on the difficulty scale and 2.0 +/- 0.6 on the concreteness scale.

Acquisition

Imaging type(s): functional fMRI BOLD, structural T1- / T2- / and T2* weighted imaging, blood flow assessment via pulsed arterial spin labeling (ASL), blood volume (CBV) assessment via dynamic susceptibility contrast imaging (contrast agent: gadolinium)

Field strength: 3 Tesla

Sequence & imaging parameters: A) Multi-echo spin-echo T2 mapping: 3D gradient spin echo (GRASE), 8 echoes with even-spaced echo times (TE): TE1 = ΔTE = 16ms; TR=251; α=90°; voxel size 2x2x3.3mm3; 35 slices (30 slices in 4 subjects); total acquisition time = 2:28min (for 35 slices)
B) Multi-echo gradient-echo T2* mapping: 12 echoes, TE1 = ΔTE = 5ms; TR=2229ms; α=30°; voxel size 2x2x3mm3; gap 0.3mm; 35 slices (30 slices in 4 subjects). Total acquisition time = 6:08min (for 35 slices).
C) Dynamic susceptibility imaging (DSC): Single-shot GRE-EPI; EPI factor 49; 80 dynamics; TR = 2.0s; α=60°; acquisition voxel size 2x2x3.5mm3; 35 slices (30 slices in 4 subjects). Injection of gadolinium-based contrast agent as a bolus after 5 dynamics, 0.1ml/kg, minimum 6ml, maximum 8ml per injection (i.e. 16ml for two injections in a row, corresponding to a full clinical dosage), flow rate: 4ml/s, additionally flushing with 25ml NaCl; total acquisition time = 2:49min (for 35

slices).
E) Pseudo-continuous arterial spin labeling (pCASL):Post-labeling delay 1800ms, label duration 1800ms; 4 background suppression pulses; 2D EPI readout; TE=11ms; TR=4500ms; α=90°; 20 slices (16 slices in one subject); EPI factor 29; acquisition voxel size 3.28x3.5x6.0mm3; gap 0.6mm; 30 dynamics including a proton density weighted M0 scan; total acquisition time = 6:00min.
F) The BOLD fMRI task-localizer was acquired using single-shot EPI, EPI factor 43; voxel size = 3.0x3.0x3.0mm3; FOV 192x192x127.8mm3; TE=30ms; TR=1.2s; α=70°; 400 dynamic scans plus two dummy scans; 40 slices; SENSE-factor = 2; MB-SENSE-factor = 2; total acquisition time: 8:05min. For susceptibility correction, a B0 field map was acquired with two echoes; TR/TE1/TE2=525ms/6.0ms/9.8ms; 40 slices; parallel acquisition; α=60°; voxel size = 3.0x3.0.3.0mm3; FOV 192x192x127.8mm3; total acquisition time: 0:35s.

Area of acquisition: Whole-brain scan

Diffusion MRI ☐ Used ☒ Not used

Preprocessing

Preprocessing software: The preprocessing and calculation of the quantitative parameter maps was performed with in-house scripts in Matlab and SPM12 (Wellcome Trust Centre for Neuroimaging, UCL, London, UK).
The BOLD fMRI localizer data were pre-processed using fMRIPrep 20.2.4 (Esteban, 2019) in a docker container, which is based on Nipype 1.6.1. This included segmentation, estimation of motion-parameters and other confounds, susceptibility distortion correction, co-registration in native T1w space and normalization to MNI152 ICBM 2mm Non-linear 6th Generation Asymmetric Average Brain Stereotaxic Registration Model (Montreal Neurological Institute, McGill University). FMRIPrep relies on FSL 5.0.9 with boundary-based registration (BBR) to register BOLD fMRI EPI time series to T1w data, FSL FAST for brain tissue segmentation and spatial normalization to standard space using ANTs 2.3.3 registration in a multiscale, mutual-information based, nonlinear registration scheme, concatenating all transforms and applying all registration steps at once. This final normalization matrix to MNI 2mm space was then applied to all quantitative mqBOLD parameter maps, after co-registering all images to native T1w space. Further, as a control for partial least squares analysis described below, classical general linear model (GLM) task-analysis was implemented following recommendations in (Esteban et al., 2020).

Normalization: All data were normalized via ANTs 2.3.3 registration in a multiscale, mutual-information based, nonlinear registration scheme, concatenating all transforms and applying all registration steps at once.

Normalization template: MNI152 ICBM 2mm Non-linear 6th Generation Asymmetric Average Brain Stereotaxic Registration Model

Noise and artifact removal: The fMRI BOLD data were corrected for head motions and bias field via fMRIPrep. For task fMRI BOLD GLMs, we used CSF and white-matter signal, dvars, framewise-displacement and translations and rotations in x-, y- and z-axis as confounds, high-pass filter of 100s and 6mm smoothing.
To exclude voxels from artifact affected brain areas, we calculated the temporal signal-to-noise ratio (tSNR) from the fMRI BOLD images per subject and voxel in standard 2mm space. We then masked out voxels that were in the lowest 15th percentile in over 66% of participants and used only masked images as an input for PLS.
For the analyses in native space, we additionally used native-space parameter maps to mask CSF-influenced areas (T2 > 90ms), susceptibility-influenced areas (R2' > 9 s-1), voxels with a high percentage of blood volume (CBV >10%, probably driven by larger veins/arteries) and voxels with T2' > 90ms, OEF > 0.9, CBF > 90ml/100g/min.

Volume censoring: n/a

Statistical modeling & inference

Model type and settings: General linear modelling on the fMRI BOLD data, first level analysis, was applied to derive brain masks in native space. In the native space analyses, we then calculated median values within each native-space ROI (output of the first level GLM, thresholded with z>3.1) per subject and tested significant differences in task compared to baseline via paired-samples two-sided t-tests, across subjects. All other statistics were based on median voxel values within a group mask, derived from partial least squares analyses in standard space, by taking the across-subjects median value per voxel in task and in baseline. Significance in parameter values between different regions was tested via independent sample permutation test (2000 permutations) on the median voxel values.

Effect(s) tested: General linear modelling, first level analysis, was applied to derive brain masks in native space. In the native space analyses, we we then tested if the quantitative parameters values changed significantly across conditions within these ROIs.
In standard space, group masks were derived via PLS analysis. We then empirically described the distribution of these voxels separately for positive and negative fMRI BOLD ROIs.
We used regression analyses to calculate Pearson's r (regression coefficient) for different classes of voxels.
We used multiple linear regression to determine the influence of each parameter (CBF, OEF and CBF) on the change in CMRO2, as well as on baseline CMRO2. Significance of the model was determined via F-tests.

Specify type of analysis: ☐ Whole brain ☐ ROI-based ☒ Both

Anatomical location(s): Anatomical locations were derived via comparison to Yeo et al. (2011) seven functional networks.

Statistic type for inference: Voxel-wise inference via partial least squares analysis on the fMRI BOLD data, see below

(See Eklund et al. 2016)

Correction

Group masks were derived via partial least squares analysis, see below, a multivariate analysis that does not rely on multiple comparison correction.

Models & analysis

n/a	Involved in the study
☒	☐ Functional and/or effective connectivity
☒	☐ Graph analysis
☐	☒ Multivariate modeling or predictive analysis

Multivariate modeling and predictive analysis

Mean-centered PLS is a data-reduction method that computes latent variables and corresponding brain patterns, which optimally relate brain signals to the experimental design, contrasting e.g. groups or conditions. We used PLSto get whole-brain significant clusters that best differentiate between the conditions. We used PLS for both the fMRI BOLD data as well as the quantitative parameter maps.
The significance of the latent variables, i.e., the entire multivariate pattern, was tested via permutation tests (3000 permutations), the reliability of the brain saliences, i.e., the voxel's contribution to the latent variables, was deduced via bootstrap resampling (3000 samples). Brain regions showing significant effects were identified via the ratio of the brain saliences to the bootstrap standard error (BSR), where a BSR > ±2 is akin to a confidence interval of 95%, if the bootstrap distribution is normal. The statistical maps were thresholded with a BSR of ±2 and only clusters with more than 30 voxels were kept for creating group masks.